Acta Oceanol. Sin., 2021, Vol. 40, No. 4, P. 39–64
https://doi.org/10.1007/s13131-021-1722-5
http://www.hyxb.org.cn
E-mail: ocean2@hyxb.org.cn

Spreading rate dependence of morphological characteristics in global oceanic transform faults

Yiming Luo[1, 2, 3, 4, 5, 7†], Jian Lin[1, 5, 6†], Fan Zhang[1, 2, 3*], Meng Wei[7]

[1] Key Laboratory of Ocean and Marginal Sea Geology, South China Sea Institute of Oceanology/Innovation Academy of South China Sea Ecology and Environmental Engineering, Chinese Academy of Sciences, Guangzhou 510301, China

[2] Southern Marine Science and Engineering Guangdong Laboratory (Guangzhou), Guangzhou 511458, China

[3] China-Pakistan Joint Research Center on Earth Sciences, Chinese Academy of Sciences-Higher Education Commission of Pakistan, Islamabad 45320, Pakistan

[4] University of Chinese Academy of Sciences, Beijing 100049, China

[5] Department of Ocean Science and Engineering, Southern University of Science and Technology, Shenzhen 518055, China

[6] Department of Geology and Geophysics, Woods Hole Oceanographic Institution, Woods Hole, MA 02543, USA

[7] University of Rhode Island, Narragansett, RI 02882, USA

Received 28 February 2020; accepted 29 June 2020

Abstract

We quantified the systematic variations in global transform fault morphology, revealing a first-order dependence on the spreading rate. (1) The average age offset of both the full transform and transform sub-segments decrease with increasing spreading rate. (2) The average depth of both the transform valley and adjacent ridges are smaller in the fast compared to the slow systems, reflecting possibly density anomalies associated with warmer mantle at the fast systems and rifting at the slow ridges. However, the average depth difference between the transform valley and adjacent ridges is relatively constant from the fast to slow systems. (3) The nodal basin at a ridge-transform intersection is deeper and dominant at the ultraslow and slow systems, possibly reflecting a lower magma supply and stronger viscous resistance to mantle upwelling near a colder transform wall. In contrast, the nodal high, is most prominent in the fast, intermediate, and hotspot-influenced systems, where robust axial volcanic ridges extend toward the ridge-transform intersection. (4) Statistically, the average transform valley is wider at a transform system of larger age offset, reflecting thicker deforming plates flanking the transform fault. (5) The maximum magnitude of the transform earthquakes increases with age offset owing to an increase in the seismogenic area. Individual transform faults also exhibit significant anomalies owing to the complex local tectonic and magmatic processes.

Key words: mid-ocean ridge, transform fault, morphology, spreading rate, transform earthquakes

Citation: Luo Yiming, Lin Jian, Zhang Fan, Wei Meng. 2021. Spreading rate dependence of morphological characteristics in global oceanic transform faults. Acta Oceanologica Sinica, 40(4): 39–64, doi: 10.1007/s13131-021-1722-5

1 Introduction

A transform fault is a major plate boundary with predominantly strike-slip motion between two adjacent plates (Wilson, 1965). Oceanic transform faults exhibit significant variability in length and age offset. Globally, the full length of a transform fault ranges from as small as 26 km (Herron transform fault) to as large as 1 099 km (Chile transform fault), and the full transform age offset is in the range of 0.69 Ma (Yaquina transform fault) to 105.8 Ma (Andrew Bain transform fault) (Boettcher and Jordan, 2004; Wolfson-Schwehr, 2015).

High-resolution bathymetry data of the last four decades have revealed the morphological complexity of oceanic transform systems. Transform faults are commonly composed of multiple subsegments, separated by fault steps, intra-transform extension basins, or intra-transform spreading centers (e.g., Searle, 1983; Fornari et al., 1989; Ligi et al., 2002; Gregg et al., 2006). This complex transform morphology might be caused by a range of tectonic and magmatic processes in the ridge-transform system (e.g., Royden et al., 1982; Lin et al., 1990; Lin and Morgan, 1992; Sempéré et al., 1993; Perfit et al., 1996; Behn et al., 2002; Gregg et al., 2006, 2007; Wolfson-Schwehr, 2015; Wei, 2019; Wolfson-Schwehr and Boettcher, 2019).

Foundation item: The foundation of Southern Marine Science and Engineering Guangdong Laboratory (Guangzhou) under contract No. GML2019ZD0205; the National Natural Science Foundation of China under contract Nos 41976064, 41890813, 41976066, 91958211, and 41706056; the scholarship of China Scholarship Council; the foundations of the Chinese Academy of Sciences under contract Nos Y4SL021001, QYZDY-SSW-DQC005, 133244KYSB20180029, and 131551KYSB20200021; the National Key Research and Development Program of China under contract Nos 2018YFC0309800 and 2018YFC0310105; the Foundation of the China Ocean Mineral Resources Research and Development Association under contract No. DY135-S2-1-04; the Guangdong Basic and Applied Basic Research Foundation under contract No. 2021A1515012227.

*Corresponding author, E-mail: zhangfan@scsio.ac.cn

†These authors contributed equally to this work.

Transform faults exhibit systematic variations in morphology that contain important information regarding the dynamics of the transforms and adjacent ridges. Almost all transform faults are associated with transform-parallel median valleys, some of which are composed of multiple topographical lows (e.g., Macdonald, 1982; Searle, 1983; Fox and Gallo, 1984; Tucholke and Schouten, 1988; Bonatti et al., 1994; Tucholke and Lin, 1994; Maia, 2019). Transform-parallel topographical highs have been observed in some transform systems either inside the transform valley (forming a median ridge) or flanking the transform fault (forming a transverse range) (Pockalny et al., 1988; 1997; Embley and Wilson, 1992; Maia, 2019). In many transform systems, the greatest depth is located near the ridge-transform intersection, forming noticeable nodal basins (e.g., Karson and Dick, 1983; Fox and Gallo, 1984; Pockalny et al., 1988). On the other hand, distinctive axial volcanic ridges are often observed at the adjacent spreading center axis and at the ridge-transform intersection (i.e., nodal highs). Nodal highs are especially well-developed in systems that have a relatively robust magma supply, such as fast- and intermediate-spreading or hotspot-influenced systems (e.g., Macdonald, 1982; Morgan and Parmentier, 1984).

The majority of studies to date have focused on investigating the morphology of individual transform faults, while quantitative analysis of the global variability in transform faults and the analysis of the dependence on the spreading rate remain limited. This lack of quantitative analyses hinders our understanding of ridge-transform dynamics.

In the present study, we quantified the global variability in transform fault morphology and investigated their dependence on the spreading rate. The investigated transform faults included examples from the ultraslow (full spreading rate<20 mm/a), slow (20–50 mm/a), intermediate (50–80 mm/a), and fast (>80 mm/a) systems (Macdonald, 1982; Dick et al., 2003) (Figs 1 and A1). The investigated systems included those at the East Pacific Rise (EPR), Pacific-Antarctic Ridge (PAR), Juan de Fuca Ridge (JDF), Southeast Indian Ridge (SEIR), Chile Rise (CR), Aden Ridge (ADEN), Central Indian Ridge (CIR), Mid-Atlantic Ridge (MAR), American-Antarctic Ridge (AAR), and Southwest Indian Ridge (SWIR) (Figs 1 and A1). We first quantified the systematic variations in the key morphological parameters and free-air gravity anomaly (FAA) of the global transform systems, including the length, age offset, depth of transform faults and adjacent ridges, depth of ridge-transform intersection, and transform width. We then analyzed the dependence of the morphological variability on the spreading rate and examined the relationship between transform morphology and earthquake magnitude. Finally, we identified anomalous transform features that deviated from the global systematics and investigated the tectonic and magmatic factors controlling the local variability.

2 Data analyses

2.1 *Data sources*

We investigated morphological parameters of transform faults through analysis of seafloor bathymetry and gravity data. We used the latest global bathymetry database with grid spacing of 15″ (Tozer et al., 2019; SRTM15_PLUS Version 2; http://topex.ucsd.edu/WWW_html/mar_topo.html), which combined the available multibeam bathymetry, shipboard soundings, and satellite altimetry-derived seafloor depth. FAA data at 1′ grid spacing were extracted from a global dataset (Sandwell et al. 2014; V26.1; http://topex.ucsd.edu/marine_grav/mar_grav.html).

2.2 *Analyses of transform parameters*

2.2.1 *Length and age offset of transform fault*

A total of 137 full transform faults were analyzed for transform length and age offset, based on the dataset of Wolfson-Schwehr (2015) (Fig. 2a1, Table A1). Among the transform faults

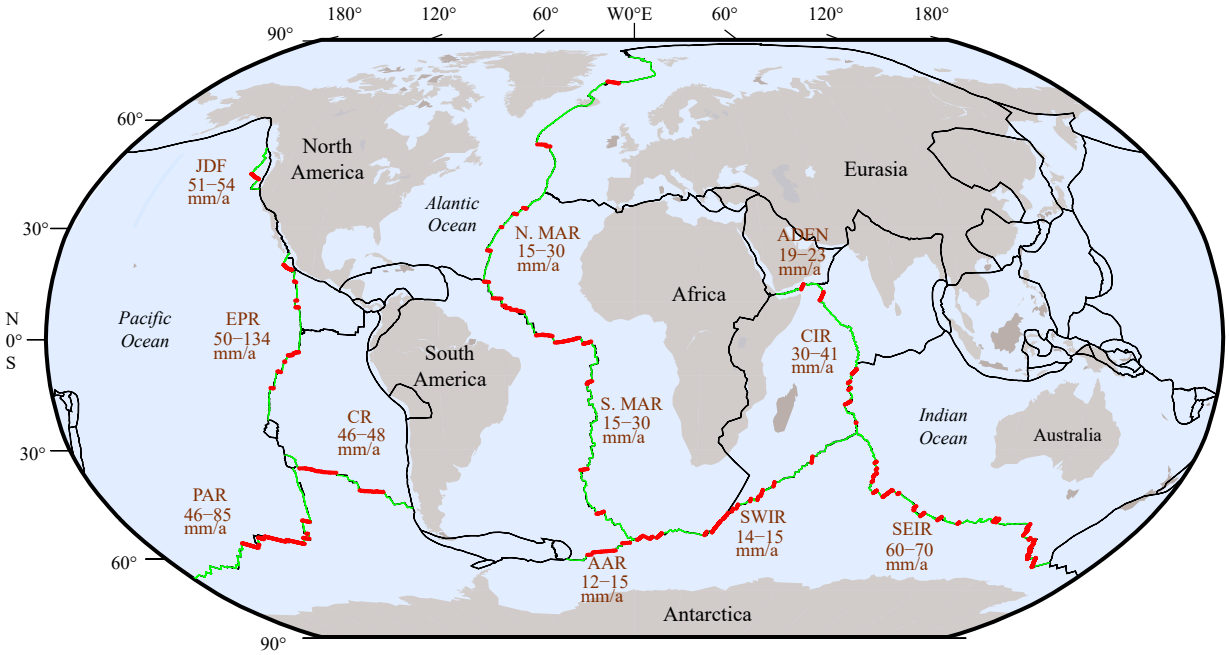

Fig. 1. Global tectonic map showing plate boundaries. Black lines denote global plate boundaries. Green lines denote the ridge-transform systems. Red lines denote the 78 transform faults with relatively good bathymetric data and were investigated in this study for morphological parameters. JDF: Juan de Fuca Ridge; EPR: East Pacific Rise; CR: Chile Rise; PAR: Pacific-Antarctic Ridge; N. MAR: North Mid-Atlantic Ridge; S. MAR: South Mid-Atlantic Ridge; AAR: American-Antarctic Ridge; SWIR: Southwest Indian Ridge; ADEN: Aden Ridge; CIR: Central Indian Ridge; SEIR: Southeast Indian Ridge.

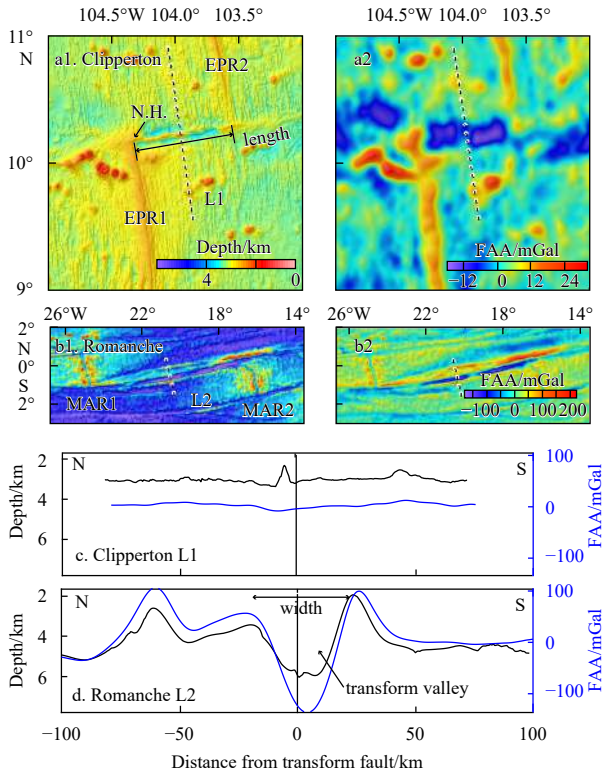

Fig. 2. Examples of transform faults. Depth (a1) and free-air gravity anomaly (FAA) (a2) of the Clipperton transform fault, as an example of a fast-spreading ridge. The depth (b1) and FAA (b2) of the Romanche transform fault, as an example of a slow-spreading ridge. Profiles of seafloor topography (black) and FAA (blue) across Clipperton (c) and Romanche (d) transform faults. Dashed lines (L1 and L2) denote locations of the across-transform profiles. EPR: East Pacific Rise; MAR: South Mid-Atlantic Ridge; N.H.: nodal high.

analyzed, a single transform fault may consist of 1–7 sub-segments according to its morphological structure (Table A1), yielding a total of 201 analyzed transform sub-segments. The transform sub-segment length (L_S) was calculated by measuring the distance between its two endpoints following a small circle (Wolfson-Schwehr, 2015). The full transform length (L_F) was then obtained by the sum of L_S for a given transform fault.

Full spreading rates (U_F) for individual transform faults (Table A1) were obtained from the Global Strain Rate Map Project (GSRM, V1.2, Kreemer et al., 2000; Wolfson-Schwehr, 2015). The corresponding full transform age offset (AO_F) is given by $AO_F = 2L_F/U_F$. Similarly, the transform sub-segment age offset (AO_S) is given by $AO_S = 2L_S/U_F$.

2.2.2 *Depth of transform valley and adjacent ridges*

We further selected 78 transform faults with relatively good bathymetric data to quantitatively analyze their morphological parameters. The cumulated length of the transform faults analyzed for morphological parameters is 16 473 km. A cumulated length of 9 304 km of the adjacent ridges was also analyzed for comparison with the associated transform faults (Fig. A1, Table A2). For a given transform fault, we first carefully traced the mid-points or the deepest points along the transform valley by visual inspection. We then calculated the average depth of the profile and defined it as the transform fault depth (black lines in Fig. A1, Table A2). We also obtained depth profiles along the axis of the adjacent ridges by visual inspection (red lines in Fig. A1, Table A2). The determination of the ridge axes was also aided by examination of the magnetic anomalies. We defined the average depth of the adjacent ridge axes as the ridge depth (Table A2). At a slow-spreading ridge (e.g., the MAR) (Fig. 2b1), we carefully tracked the deepest points of the axial valley or a small central volcanic high. At a fast-spreading ridge (e.g., the EPR) (Fig. 2a1) or a hotspot-influenced ridge, we carefully tracked the axial topographic high or a small central depression.

2.2.3 *Depth of ridge-transform intersection*

We carefully examined the 3D topography of a ridge-transform intersection to determine whether it is associated with a local basin (i.e., nodal basin, Fig. A2a1) or a topographical high (i.e., nodal high, Fig. 2a1). For a local basin, we found the deepest point by visual inspection and defined its depth as the nodal basin depth (Table A3). Similarly, for a local topographic high, we located the shallowest point by visual inspection and defined its depth as the nodal high depth.

2.2.4 *Width of transform fault*

We calculated the widths of 44 transform faults with relatively simple structure. We first traced the peaks of the two conjugate transform walls. We then calculated the distance between the two conjugate peak points at the mid-point of the transform fault. The measured distance was defined as the width of the transform fault (Fig. 2d, Table 2).

2.2.5 *Lithospheric thickness*

To the first-order, the oceanic plate adjacent to a transform fault can be approximated as a thermal boundary layer that thickens as the square root of the lithospheric age (Turcotte and Schubert, 2014). Thus, the lithospheric plate thickness (h_L) at the mid-point of a full transform fault is shown by $h_L = 2.32\sqrt{\kappa\tau_{1/2}}$, where $\kappa = 10^{-6}$ m^2/s is the thermal diffusivity, and $\tau_{1/2} = L_F/U_F$ is lithospheric age at the mid-point of the transform fault.

2.2.6 *Moment magnitude of transform earthquake*

The maximum earthquake moment magnitudes of global transform faults (M_w^{max}, Table A1) were obtained by Wolfson-Schwehr (2015) and Wolfson-Schwehr and Boettcher (2019) from the Global Centroid Moment Tensor Project (Dziewonski and Anderson, 1981; Ekström et al., 2012). A 50 km wide rectangular polygon centered on a transform fault was used to define the earthquakes of a given transform fault (Wolfson-Schwehr, 2015).

2.2.7 *Seismogenic area*

The seismogenic area (A_t) of a transform fault was calculated by integrating the cross-sectional area of the transform wall above the 600°C isotherm (Table A1, Boettcher and Jordan, 2004; Wolfson-Schwehr, 2015).

3 Results

3.1 *Characteristic topography and gravity anomaly of transform fault*

The oceanic transform faults exhibit common topographical characteristics, including a transform valley, high topography on the flanks (Figs 2 and A2), and a nodal high (Fig. 2a1) or nodal basin (Fig. A2b1) at the ridge-transform intersection. The sea-

floor topography remains relatively constant away from the transform fault. Across-transform topographical variations are relatively small (1–2 km) and narrow (20–50 km) in the fast (e.g., Clipperton, Figs 2a1 and c) and intermediate (e.g., Zeehaen, Figs A2a1 and c) systems, but are larger (up to ~3.5 km) and wider (up to ~100 km) in the slow (e.g., Romanche, Figs 2b1 and d) and ultraslow (e.g., Du Toit, Figs A2b1 and d) systems.

We also examined the FAA that reflects the integrated gravitational effects of the seafloor topography and density anomalies beneath the seafloor (Figs 2a2–b2 and A2a2–b2). Most of the prominent topographical features, including the transform valley and flanking high, are visible in the FAA (Figs 2c–d and A2c–d).

3.2 *Length of transform fault*

Among the 137 transform faults that we examined for transform length, 23, 64, and 38 are located at the ultraslow, slow, and intermediate systems, respectively, while 12 are at the fast systems (Fig. 3). At the fast systems, the Menard transform fault (208 km) at the PAR has the greatest length (Fig. 4a1). At the intermediate systems, the Tasman transform fault (625 km) at the SEIR has the greatest length (Fig. 4a2), which is composed of 5 sub-segments, with lengths of 90 km, 218 km, 62 km, 173 km, and 82 km, respectively. At the slow systems, the Chile transform fault (1 099 km) at the CR has the greatest length (Fig. 4a3), which consists of 3 sub-segments, with lengths of 493 km, 186 km, and 420 km, respectively. At the ultraslow systems, the Andrew Bain transform fault (706 km) at the SWIR has the greatest length (Fig. 4a4), which consists of 3 sub-segments, with lengths of 87 km, 148 km, and 471 km, respectively (Fig. 4).

Most of the transform faults are within 400 km in full length (Figs 4a1–a4). Ultra-long transform fault systems (full length> 400 km) are located at the intermediate, slow, and ultraslow systems (Figs 4a2–a4), including the George V (414 km), Tasman (625 km), Tharp (462 km), Doldrum (726 km), Romanche (878 km), Saint Paul (589 km), Chile (1 099 km), Valdavia (599 km), Andrew Bain (706 km), and Bullard (526 km). Transform sub-segments with lengths over 400 km include the Tharp, Chile A and C, Romanche, Bullard B, and Andrew Bain C (Figs 4b2–b4, Table A1).

3.3 *Age offset of transform fault*

The full transform age offset (Figs 5a1–a4) and transform sub-segment age offset (Figs 5b2–b4) increase with decreasing spreading rate. Transform faults with age offset greater than 40 Ma are observed mainly at ultraslow and slow systems, including the Andrew Bain, Bullard, Shackelton, Doldrum, Romanche, Saint Paul, and Chile (Figs 5a3–a4 and 6c). Transform sub-segments with age offsets greater than 40 Ma include the Andrew Bain C, Bullard B, Shackelton, and Romanche (Figs 5b3–b4 and 6d, Table A1). The average full/sub-segment age offset decreases with increasing spreading rate (Figs 6c and d, Table 1). Furthermore, the standard deviation values of the transform length and age offset are in general greater for the ultraslow and slow systems than the intermediate and fast systems (Fig. 6, Table 1).

3.4 *Depth of ridge-transform system*

Along the global ridge-transform system, transform faults are consistently deeper than the adjacent ridges (Figs 7a1–k1). Correspondingly, the FAA is consistently more negative at the transform faults than the adjacent ridges (Figs 7a2–k2 and A3). Regions affected by hotspots are associated with shallower seafloor and more positive FAA, e.g., the Iceland and Azores (Figs 7h1 and

Table 1. Average and standard deviation (STD) values of morphological parameters of oceanic transform faults

Parameter*	Average/STD			
	Ultraslow	Slow	Intermediate	Fast
L_F/km	185.3/152.7	172.9/201.1	158.2/145.5	108.1/49.5
L_S/km	163.9/118.3	122.9/120.4	108.6/98.2	44.7/38.1
AO_F/Ma	29.9/26.6	11.0/12.5	4.7/4.3	2.1/1.2
AO_S/Ma	26.4/22.2	7.8/8.2	3.2/2.8	0.8/1.0
D_T/km	4.60/0.85	4.27/0.59	3.53/0.71	3.42/0.36
D_R/km	3.44/0.78	3.68/0.44	2.86/0.57	2.72/0.23
D_T–D_R/km	–1.16/0.60	–0.59/0.52	–0.66/0.60	–0.70/0.39
$D_{N.H.}$/km	3.25/0.64	3.27/0.60	2.75/0.44	3.01/0.24
$D_{N.B.}$/km	4.50/0.73	3.95/0.57	3.68/0.63	3.39/0.14

Note: * L_F: full transform length; L_S: transform sub-segment length; AO_F: full transform age offset; AO_S: transform sub-segment age offset; D_T: depth of transform fault; D_R: depth of adjacent ridges; D_T–D_R: depth difference of transform fault and ridge; $D_{N.H.}$: depth of nodal high; $D_{N.B.}$: depth of nodal basin.

Table 2. Transform width at the mid-point of 44 investigated transform faults

Transform fault	Width/km	Transform fault	Width/km	Transform fault	Width/km	Transform fault	Width/km
Alula Fartak	29	Clipperton	25	Islas Orcadas	32	SEIR 120E	14
Amsterdam	13	Conrad	38	Kane	26	SEIR 88E	10
Ascension	36	Du Toit	35	MAR 15 20	27	SEIR 96E	18
Atlantis	30	Euroka	19	Marie Celeste	28	Shaka	36
Atlantis II	45	Falkland	26	Menard	12	Tharp	20
Blanco	15	Garrett B	22	Oceanographer	27	Valdavia	17
Bouvet	36	Geelvinck	20	Orozco	16	Vema	37
Bullard A	36	Gemino	36	Rivera	23	Vema II	27
Bullard B	40	Hayes	27	Romanche	50	Vlamingh	36
Chain	36	Heezen	20	SEIR 100E	18	Wilkes	25
CIR 12°12′	30	Hillegom's Hole	14	SEIR 106E	25	Zeewolf	21

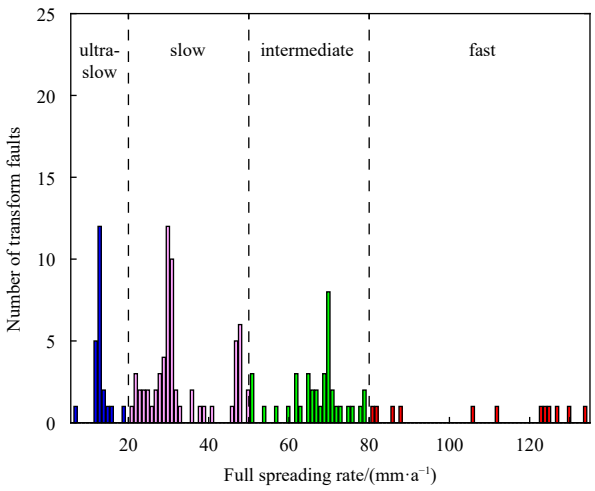

Fig. 3. Distribution of full spreading rate of global transform faults. Colors: red (fast), green (intermediate), magenta (slow), and blue (ultraslow).

h2). When modeled by Gaussian distribution, the mean depth and FAA of the transform faults are consistently greater than that of the adjacent ridges (Figs 8 and A3).

The average depth of transform faults decreases with increasing spreading rate (Fig. 9a, Table 1). The average depth of the adjacent ridges also decreases with increasing spreading rate (Fig. 9b, Table 1). However, the average depth difference between the transform faults and adjacent ridges is relatively constant, and is only slightly greater at the ultraslow system (Fig. 9c).

The spreading rate dependence of the transform and ridge depth could be associated with a combination of factors including thermal structure and dynamic topography. First, at a given distance from the ridge axis, the mantle temperature is higher and thus the density is lower at a faster ridge (Turcotte and Schubert, 2014). The overall higher mantle temperature also leads to a greater degree of partial melting at a faster ridge. Both the thermal and partial melting density anomalies contribute to shallower seafloor (Magde and Detrick, 1995). Second, slow-spreading ridges are often associated with an axial rift valley that could be caused by hydraulic head loss in the upwelling mantle (Sleep, 1969; Sleep and Biehler, 1970), tectonic faulting (Shaw and Lin, 1996), and lithospheric necking (e.g., Tapponnier and Francheteau, 1978; Lin and Parmentier, 1989; Chen and Morgan, 1990).

3.5 *Depth of ridge-transform intersection*

The average depth of the global nodal basins (Fig. 10a) is 0.38–1.25 km deeper than those of the nodal highs (Fig. 10b, Table A3). The nodal high is dominant at the fast (Fig. 10c) and intermediate (Fig. 10d) systems. In contrast, nodal basin is prevalent at the slow (Fig. 10e) and ultraslow (Fig. 10f) systems.

The average depths of nodal highs are relatively constant (3.25–3.27 km) for the slow and ultraslow systems, but slightly smaller (2.75–3.01 km) for fast and intermediate systems (Fig. 10a, Table 1). The average depths of nodal basins decrease with increasing spreading rate (Fig. 10b, Table 1).

The commonly observed nodal basins at slow and ultraslow systems might reflect a decrease in ridge-axis magma supply (Fox and Gallo, 1984) and viscous resistance to mantle upwelling by the cold transform wall (Sleep, 1969; Sleep and Biehler, 1970). In contrast, nodal highs might appear at ridge systems where ro-

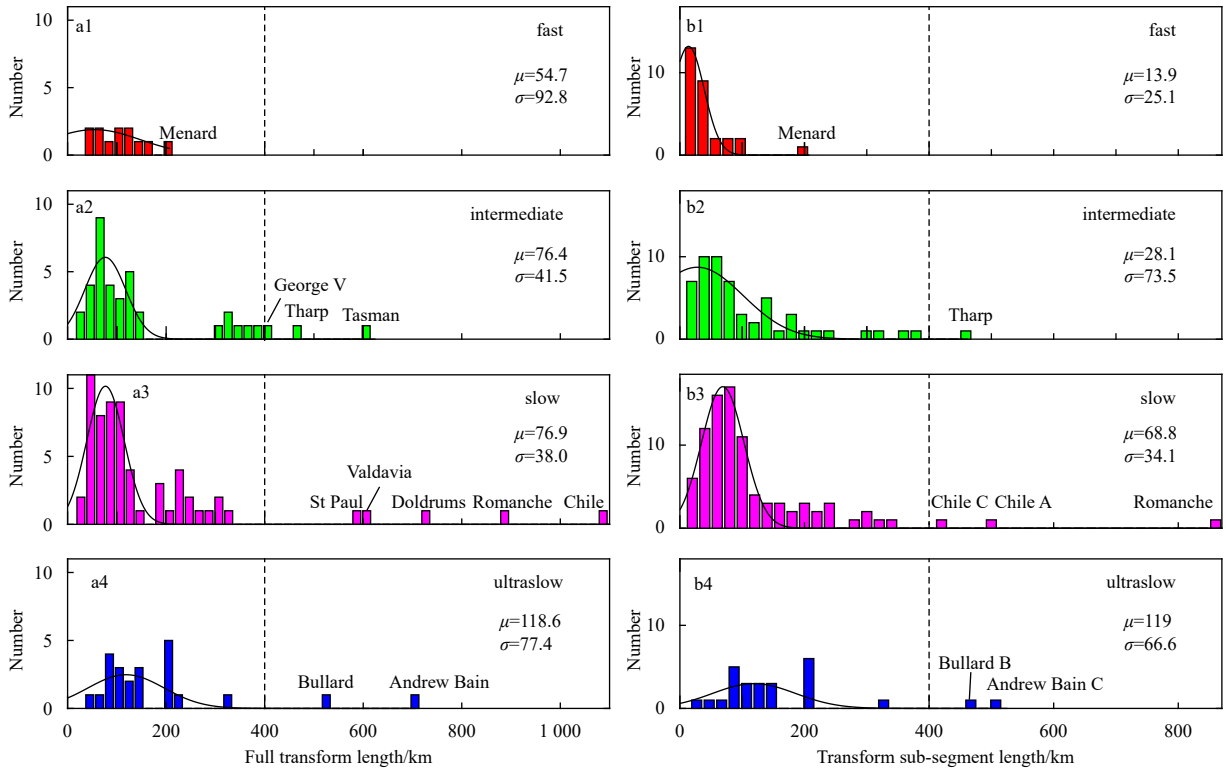

Fig. 4. Distribution of full transform length (a1–a4) and transform sub-segment length (b1–b4). Red: fast; green: intermediate; magenta: slow; and blue: ultraslow. μ and σ of each panel denote mean and standard deviation of the best-fitting Gaussian distribution, respectively.

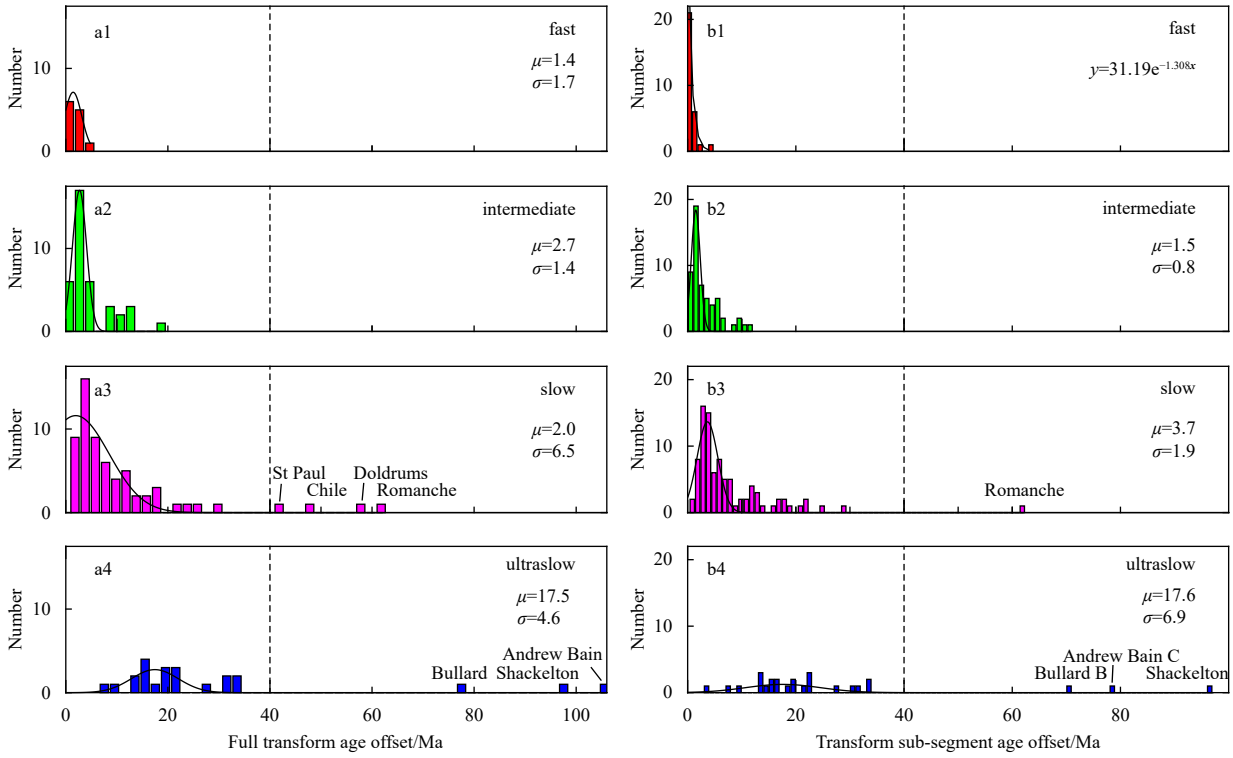

Fig. 5. Distribution of full transform age offset (a1–a4) and transform sub-segment age offset (b1–b4). Red: fast; green: intermediate; magenta: slow; and blue: ultraslow. μ and σ of each panel denote mean and standard deviation of the best-fitting Gaussian distribution, respectively.

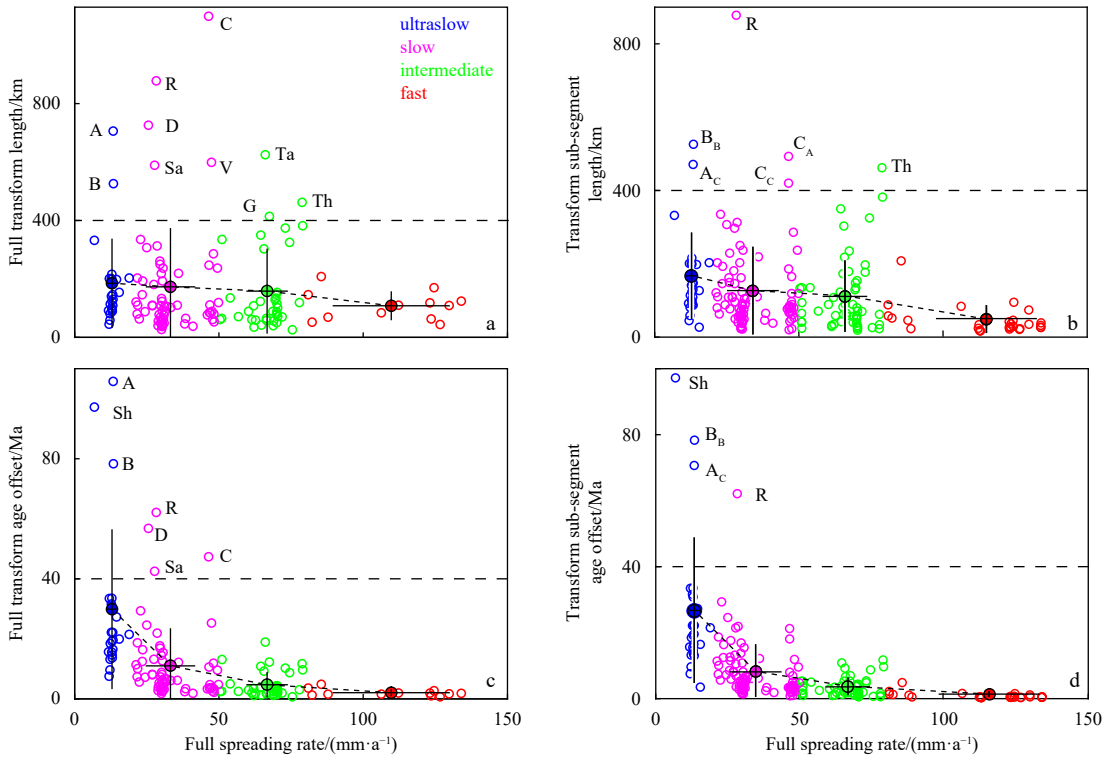

Fig. 6. Full transform length (a), transform sub-segment length (b), full transform age offset (c), and transform sub-segment age offset versus full spreading rate (d). Filled circles and black lines show average values and standard deviations for each spreading rate, respectively. A: Andrew Bain; A_C: Andrew Bain Segment C; B: Bullard; B_B: Bullard Segment B; C: Chile; C_A: Chile Segment A; C_C: Chile Segment C; D: Doldrums; G: George V; R: Romanche; Sa: Saint Paul; Sh: Shackelton; Ta: Tasman; Th: Tharp; V: Valdavia. Red: fast; green: intermediate; magenta: slow; and blue: ultraslow.

bust axial volcanic ridges extend toward ridge-transform intersections (Fig. 2, Table A3).

3.6 *Width of transform fault*

In general, the transform width (w) decreases with increasing spreading rate for the ultraslow (29–45 km), slow (17–50 km), intermediate (10–36 km), and fast (12–25 km) systems (Fig. 11a). Ultra-wide transform systems with widths greater than 40 km include the Romanche (w of 50 km, age offset of 62.1 Ma) of the MAR, Atlantis II (45 km, 33.4 Ma) of the SWIR, and Bullard B (40 km, 78.3 Ma) of the AAR (Table 2). In general, the transform width is systematically greater for systems of larger age offset (Fig. 11a). In a special case when a transform valley is bounded by two inward-dipping normal faults, the transform width (w) is expected to depend on the plate thickness (h_L) (Fig. 11b inset). However, other factors might also control the transform fault width, including multiple transform faults and extension episodes.

4 Discussion

4.1 *Unusual transform systems*

While the investigated transform parameters show first-order dependence on spreading rate, the variation within each spreading rate group is large, especially for the slow and ultraslow systems (Figs 6, 9 and 10, Table 1). Furthermore, for each of the investigated parameters, multiple examples of major exceptions were observed. In particular, several transform systems have anomalies in more than one parameter (Table 3). These major anomalies reveal unusually complex local tectonic and magma variability.

4.1.1 *Transform complexity caused by plate motion changes*

The Romanche transform fault (Fig. 2b1) is one of the longest (878 km) and deepest (7.9 km) transform systems on Earth (Bonatti et al., 1994; Wolfson-Schwehr, 2015). It is associated with unusually large values in length (Figs 6a and b), age offset (Figs 6c and d), transform depth (Fig. 9a), and transform width (Fig. 11a). The active transform boundary, previously located in the northern valley, had migrated southward to its present location a few million years ago and formed ridges inside the transform domain. The morphological complexity of the Romanche transform was probably caused by alternating across-transform transtension and transpression induced by plate motion changes (Bonatti et al., 1994; Searle et al., 1994; Ligi et al., 2002).

For the Andrew Bain transform at the SWIR, Sclater et al. (2005) similarly proposed that its morphological complexity was

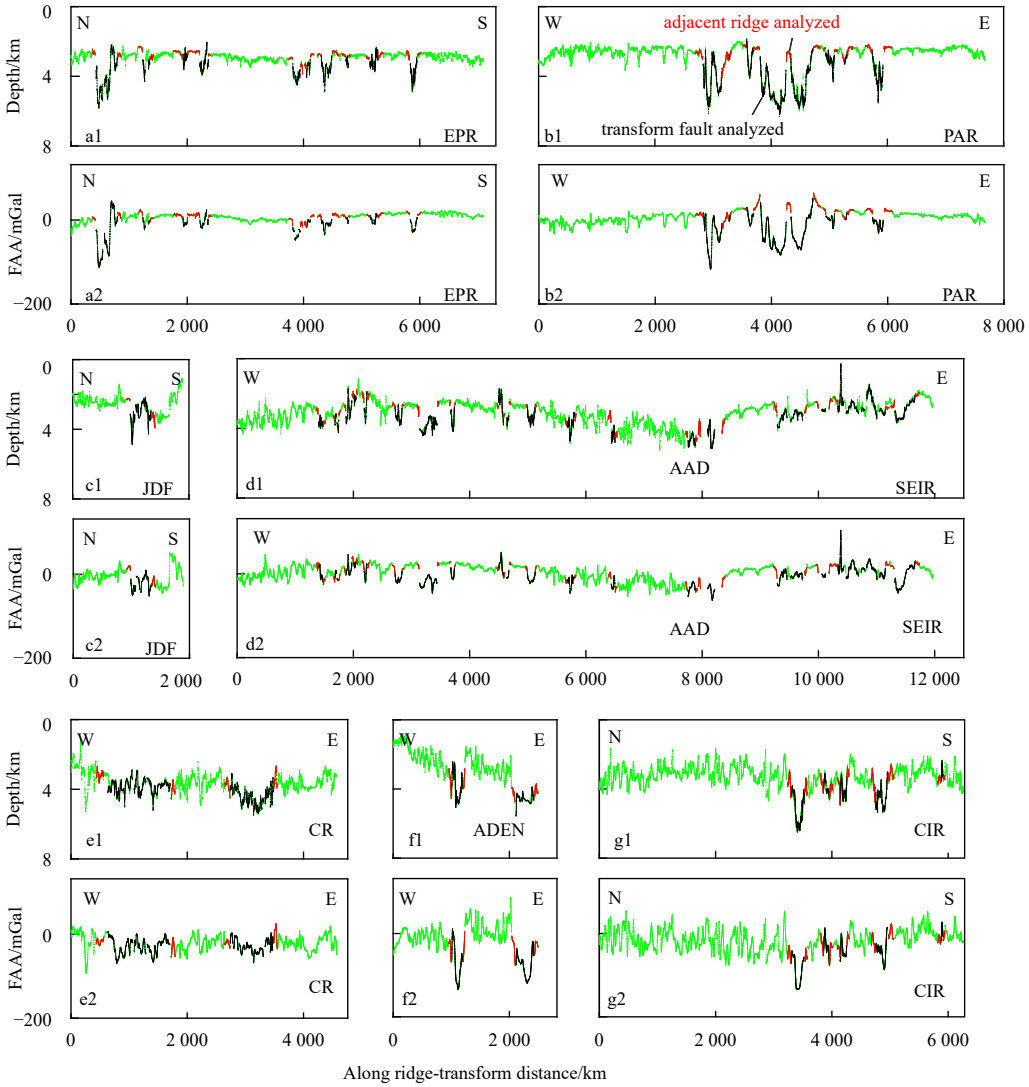

Fig. 7.

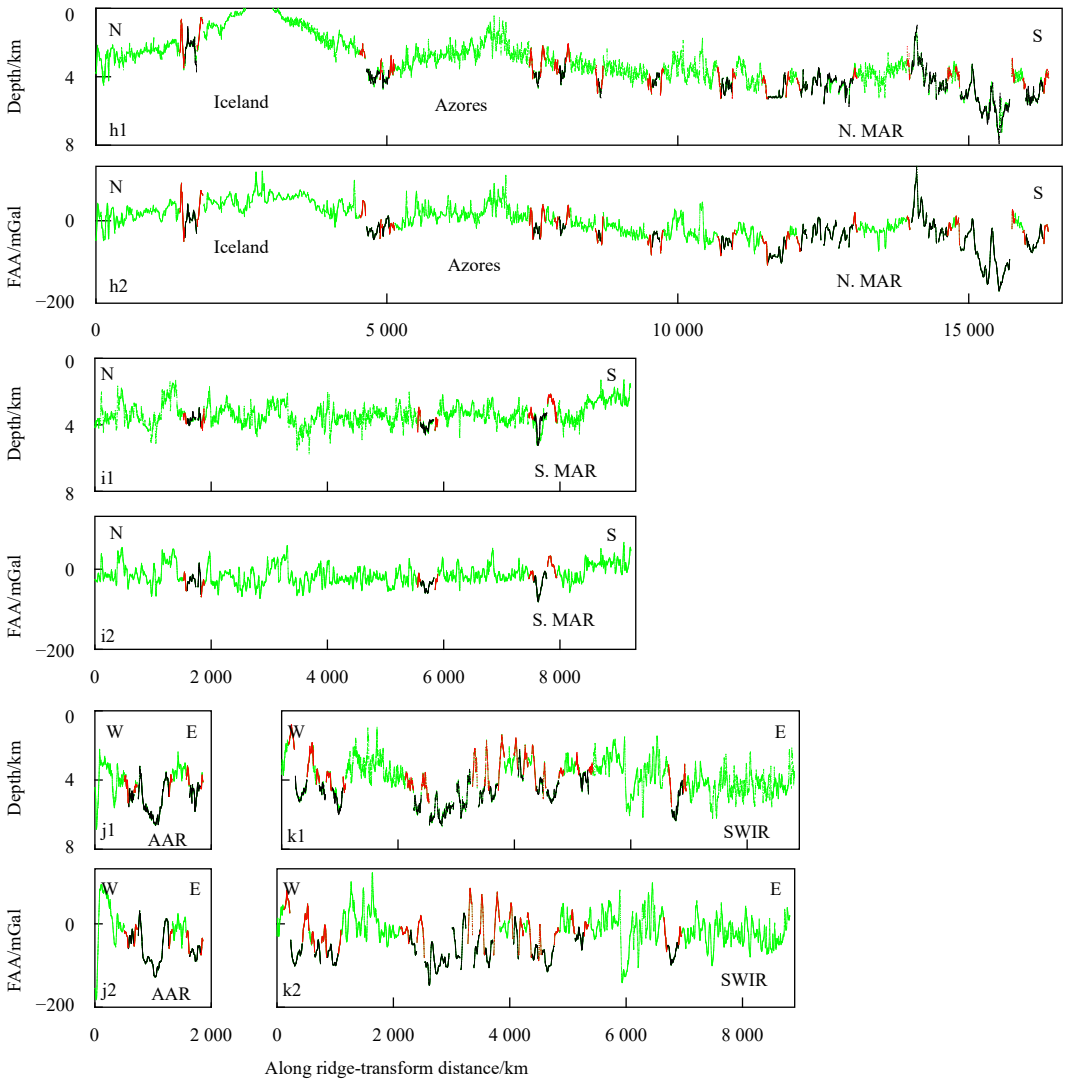

Fig. 7. Along ridge-transform profiles of seafloor depth (a1–k1) and FAA (a2–k2) of the global ridge-transform systems. Green lines denote along ridge-transform profiles, using the global bathymetry dataset. Black lines denote the 78 transform faults with relatively good bathymetric data and thus selected for detailed analysis of morphological parameters. Red lines denote ridge adjacent to the 78 analyzed transform faults. AAD: Australian-Antarctic Discordance; EPR: East Pacific Rise; PAR: Pacific-Antarctic Ridge; JDF: Juan de Fuca Ridge; SEIR: Southeast Indian Ridge; CR: Chile Rise; ADEN: Aden Ridge; CIR: Central Indian Ridge; N. MAR: North Mid-Atlantic Ridge; S. MAR: South Mid-Atlantic Ridge; AAR: American-Antarctic Ridge; SWIR: Southwest Indian Ridge.

a response to transtension across the transform system, causing multiple transform sub-segments (Fig. A4a). Geodynamic modeling illustrated the possibility of alternating activation of multiple sub-parallel strike-slip faults within a wide transform domain, such as those observed in the Romanche and Andrew Bain systems (Ligi et al., 2002).

In addition to the Romanche and Andrew Bain systems, there are several examples of major morphological anomalies that might have been caused by across-transform transtension and/or transpression. For example, it was proposed that the Atlantis II transform (Fig. A4b) has experienced transtension for 12 million years due to plate rotation of 10° since ~19.5 Ma (Baines et al., 2003); the Bullard transform (Fig. A4c) was subjected to transpression during the early Miocene period (Livermore et al., 1991); and the Heezen and Tharp transforms at the PAR had undergone transtension since 12 Ma, resulting in the formation of extra deep transform valleys (Fig. A4d) (Lonsdale, 1994; Croon et al., 2008).

4.1.2 *Transform complexity caused by hotspot influence*

The Bouvet transform fault at the SWIR is located close to the Bouvet hotspot (Fig. A4e). The average depth of the eastern ridge segment is smaller than that of the conjugate western segment by about 1 km (Fig. 9b). Such a transform-ridge depth difference (–2.7 km) is about 1.6 km greater than the global average value for the corresponding spreading rate (Fig. 9c). Thus, the observed anomalies in the depth difference between ridge and transform fault of the Bouvet system are attributed to excess magma, thicker crust, and shallower seafloor at the ridge axis due to hotspot-ridge interaction (Georgen et al., 2001).

The Jan Mayen transform fault at the northern MAR connects the Jan Mayen Ridge and is located north of Iceland (Figs A1e and A4f). The depths of the Jan Mayen transform fault (Fig. 9a) and the adjacent ridges (Fig. 9b) are exceptionally shallow and are interpreted as the result of the excess magma supply from the Jan Mayen hotspot (Zhang et al., 2020).

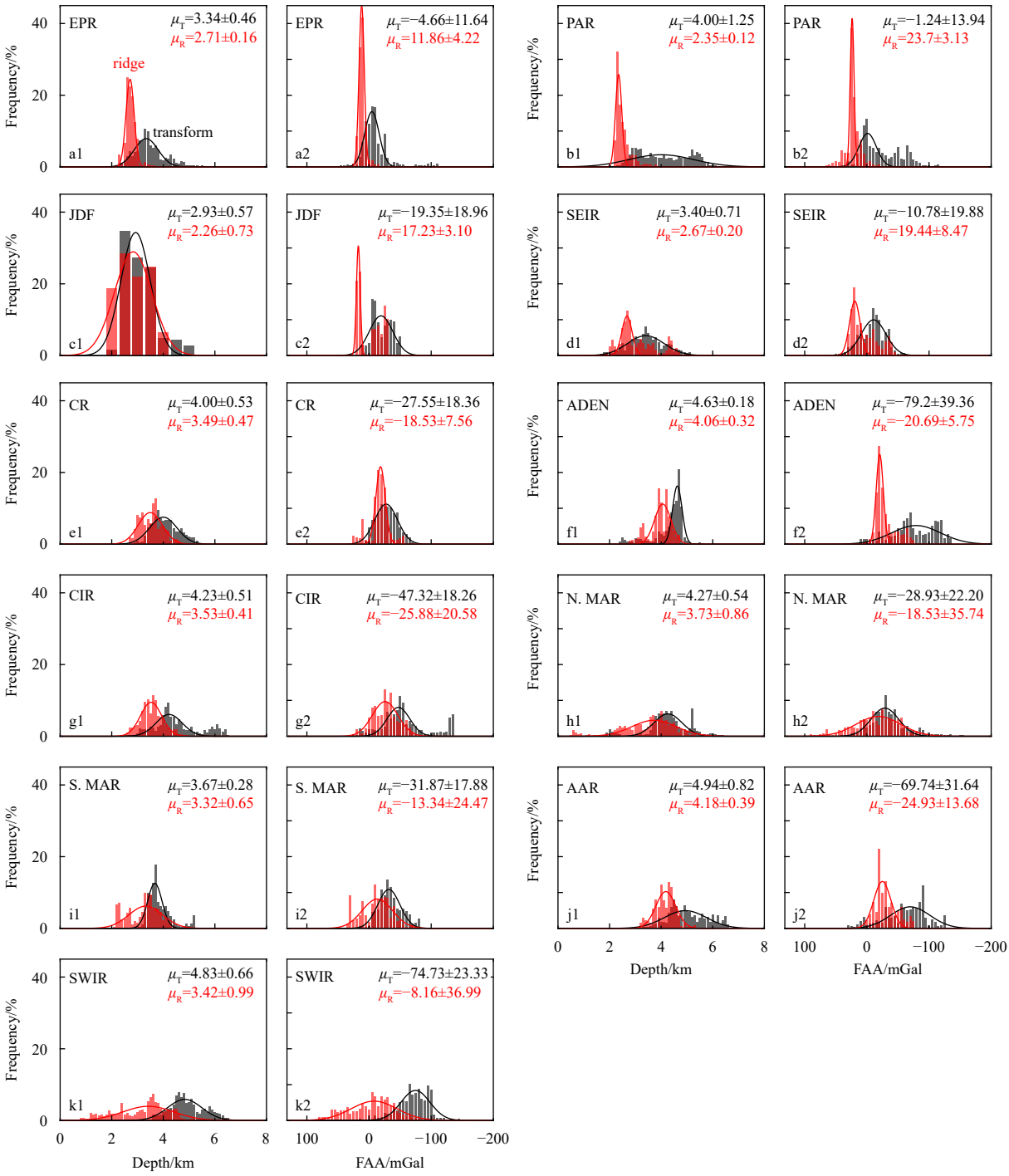

Fig. 8. Frequency distributions of seafloor depth (a1–k1) and FAA (a2–k2) of transform faults (black) and adjacent ridges (red) of the 78 analyzed transform systems. EPR: East Pacific Rise; PAR: Pacific-Antarctic Ridge; JDF: Juan de Fuca Ridge; SEIR: Southeast Indian Ridge; CR: Chile Rise; ADEN: Aden Ridge; CIR: Central Indian Ridge; N. MAR: North Mid-Atlantic Ridge; S. MAR: South Mid-Atlantic Ridge; AAR: American-Antarctic Ridge; SWIR: Southwest Indian Ridge. μ_T and μ_R of each panel denote mean of the best-fitting Gaussian distribution of transform faults and ridges, respectively.

4.2 *Maximum magnitude of transform earthquake*

The M_w^{max} in general increases with increasing transform length (Fig. 12a) for length less than 300 km, as well as with increasing age offset (Fig. 12c) for age offset less than 40 Ma. At systems of greater transform length and age offset, the M_w^{max} increases only slightly.

M_w^{max} increases with increasing A_t (Fig. 12d), which is consistent with theoretical consideration. The moment magnitude (M_w) of an earthquake is defined as $M_w=2/3\times\log_{10}(\mu\times A_t\times S)-10.7$ (Kanamori, 1977), where $\mu=3\times10^{10}$ Pa is the rock rigidity, and S is the average slip during an earthquake. Therefore, M_w^{max} should increase with increasing A_t and S (Fig. 12d). Roland et al. (2010) proposed that the base of the seismogenic area (600°C isotherm) is nearly flat, which differs from the half-space cooling model

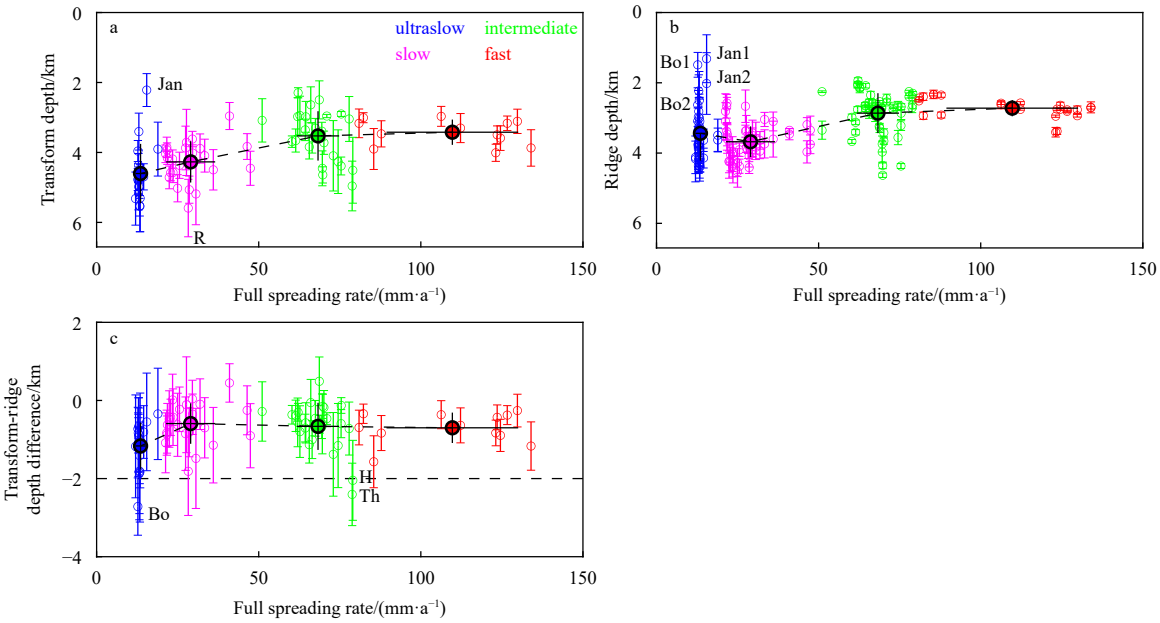

Fig. 9. Transform fault depth (a), adjacent ridges depth (b), and transform-ridge depth difference (c) versus full spreading rate of the 78 analyzed transform systems. Open circles and thin lines denote depth and standard deviation, respectively. Filled circles and black lines show average depth and standard deviation for each spreading rate, respectively. Red: fast; green: intermediate; magenta: slow; and blue: ultraslow. Bo: Bouvet; H: Heezen; Jan: Jan Mayen; R: Romanche; Th: Tharp.

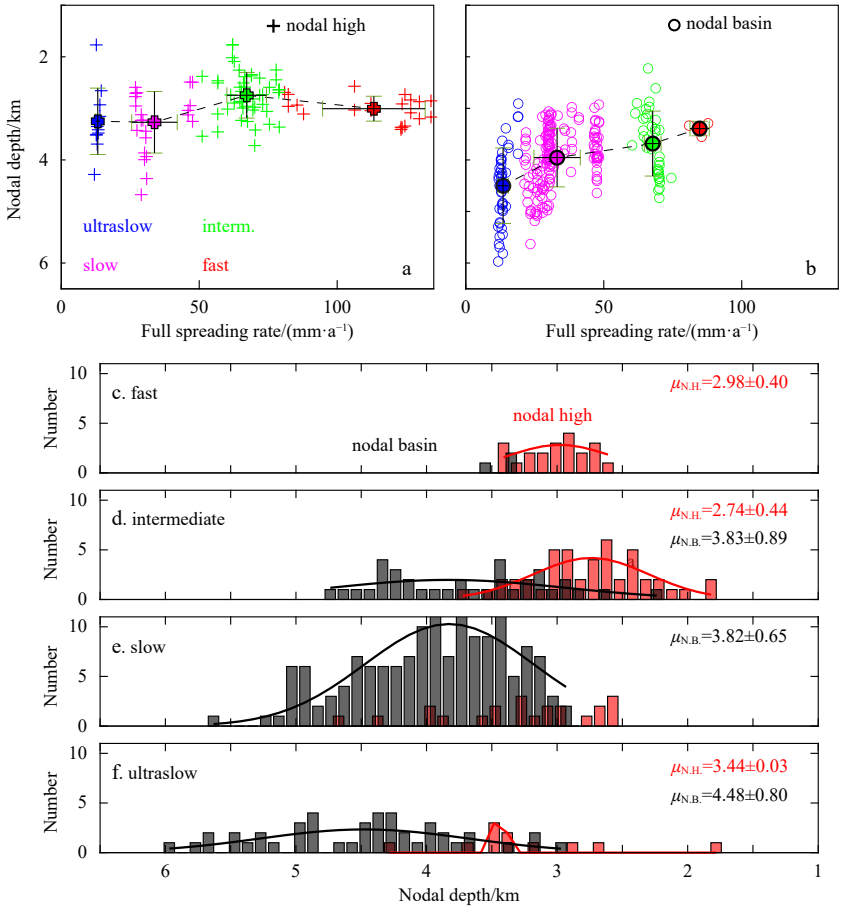

Fig. 10. Depth of nodal high (a) and nodal basin (b) versus full spreading rate. In a and b, red: fast; green: intermediate; magenta: slow; and blue: ultraslow. Frequency distribution of the depth of nodal basin (black) and nodal high (red) for each spreading rate group. Curves denote the best-fitting Gaussian distribution. $\mu_{N.H.}$ and $\mu_{N.B.}$ of each panel denote mean of the best-fitting Gaussian distribution of nodal highs and nodal basins, respectively.

Table 3. Examples of transform faults with major anomalies

Transform fault	Ridge system	L_F>400 km	L_S>400 km	AO_F>40 Ma	AO_S>40 Ma	Depth anomalies	Width>40 km
Andrew Bain	SWIR	√	√	√	√		
Atlantis II	SWIR						√
Bouvet	SWIR					√	
Bullard	AAR	√	√	√	√		√
Shackelton	AAR			√	√		
Doldrums	MAR	√		√			
Romanche	MAR	√	√	√	√	√	√
Saint Paul	MAR	√		√			
Jan Mayen	MAR					√	
Chile	CR	√		√			
Valdavia	CR	√					
George V	SEIR	√					
Tasman	SEIR	√					
Heezen	PAR					√	
Tharp	PAR	√				√	

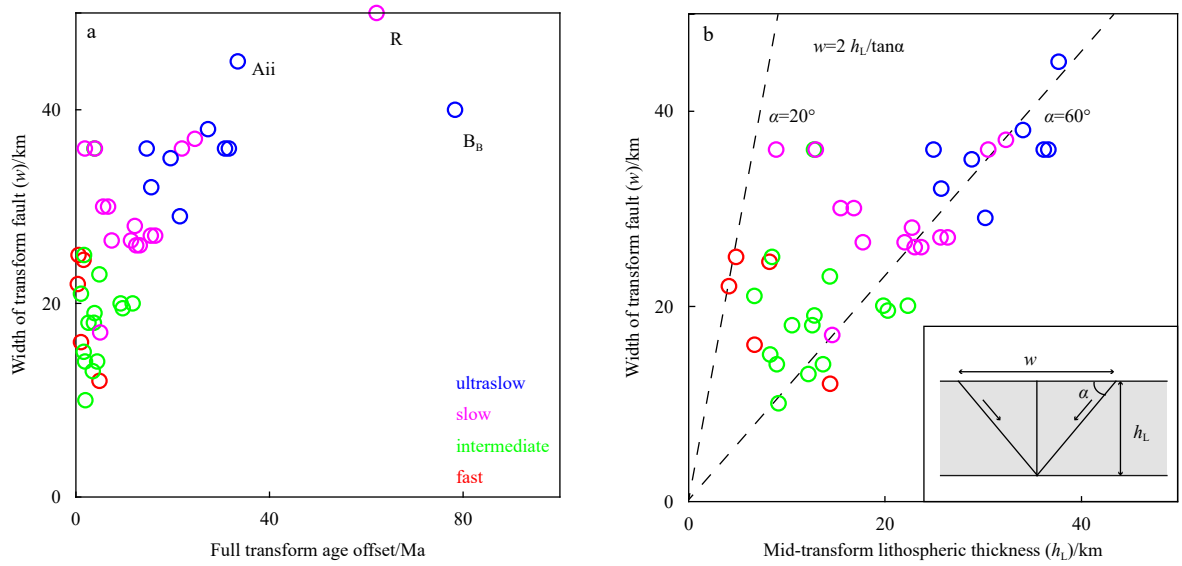

Fig. 11. Correlation of width of transform faults with full transform age offset (a), and mid-transform lithospheric thickness (b). Red: fast; green: intermediate; magenta: slow; and blue: ultraslow. In b, gray layer shows a lithospheric plate with a thickness of h_L. This corresponds to a special case when a transform valley is bounded by two inward-dipping conjugate normal faults with dip angle (α). The dashed lines show the expected dependence of the transform width (w) on plate thickness, with a dipping angle of 20° and 60°, respectively. Aii: Atlantis II; B_B: Bullard B; R: Romanche.

(Boettcher and Jordan, 2004). Therefore, using the half-space cooling model might underestimate A_t and M_W.

M_w^{max} decreases moderately with increasing spreading rate (Fig. 12b). Bird et al. (2002) also found that the corner magnitude of transform earthquakes decreases with increasing spreading rate. Such spreading rate dependence could be due to multiple factors. First, the age offset is in general smaller for fast systems, leading to smaller A_t and thus M_w. Second, the lizardite mineral phases might exist only at transforms with slow rates, where serpentinization might be present at transform faults. The presence of lizardite in slow-spreading systems might promote unstable sliding along the transform fault, leading to large transform earthquakes (Bird et al., 2002).

5 Conclusions

Our quantitative analysis of the morphological parameters of global oceanic transform faults yielded the following key results.

(1) The age offset of transform faults and transform sub-segments decrease with increasing spreading rate.

(2) Both transform faults and adjacent ridges are shallower at the fast-spreading compared to the slow-spreading systems, likely reflecting density anomalies associated with warmer mantle at the fast systems and rifting at the slow ridges. However, the average depth difference between the transform fault and adjacent ridges is relatively constant from the slow- to fast-spreading systems.

(3) Nodal basins are mostly observed at the slow and ultraslow systems; whereas nodal highs are prevalent at the fast and intermediate systems. The nodal basin is possibly related to reduced ridge-axis magma supply and stronger viscous resistance to mantle upwelling by the cold transform wall, whereas a nodal high is formed where the robust ridge-axis volcanic ridges extend toward a transform fault.

(4) The average transform width is greater at a larger age offset, possibly reflecting greater effective elastic thickness of the deforming plates flanking the transform valley.

(5) The average maximum moment magnitude of the transform earthquakes increases with the transform length, age offset,

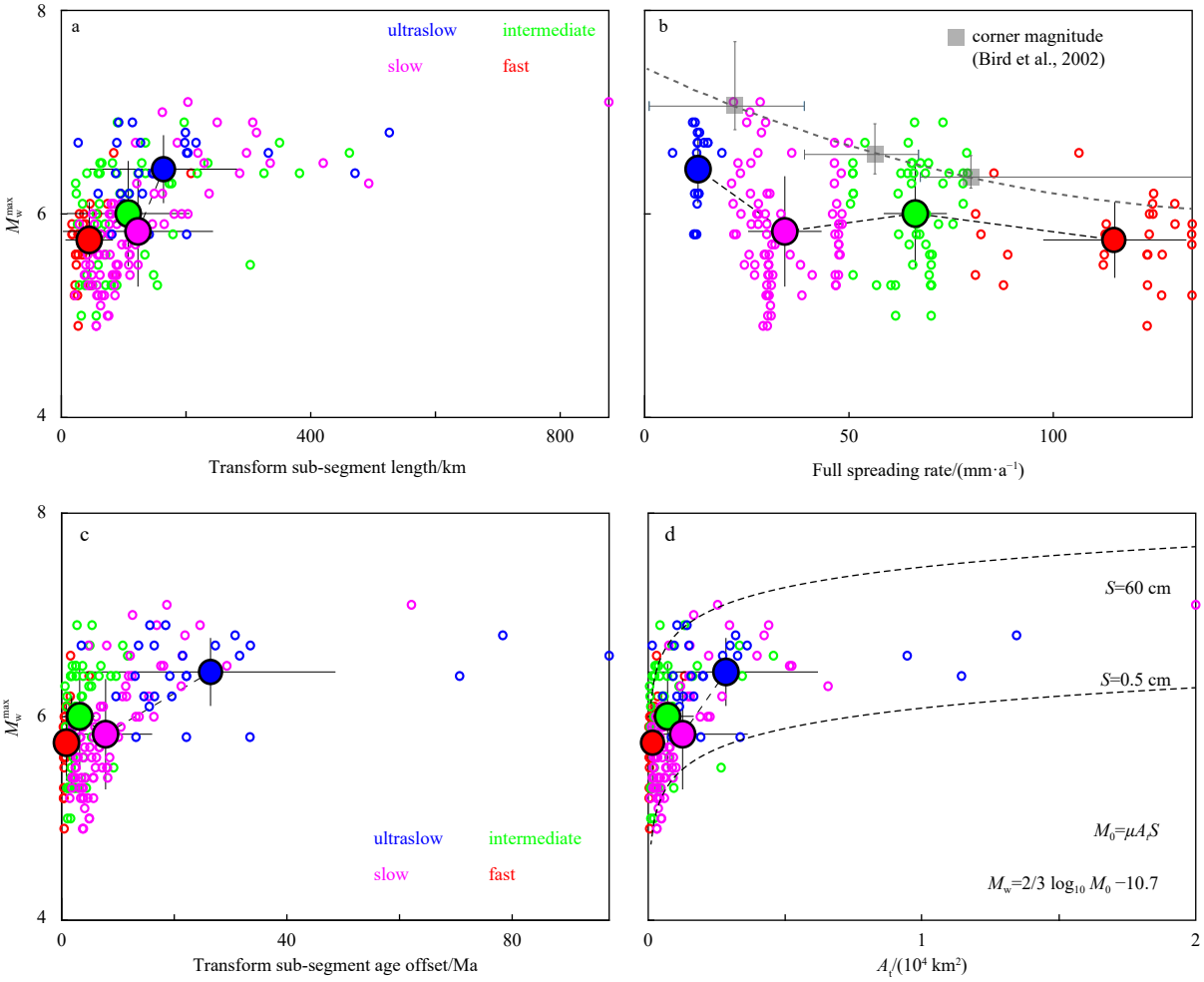

Fig. 12. The maximum moment magnitude (M_w^{max}) of the transform earthquake versus transform sub-segment length (a), full spreading rate (b), transform sub-segment age offset (c), and seismogenic area (d, A_t). Open circles denote Mwmax of the global transform faults. Filled circles and black thin lines show the average M_w^{max} and standard deviations for each spreading rate. Color definition is the same as in Fig. 3. Gray squares in b show the empirical corner magnitudes of three subgroups by maximum likelihood. The solid curve denotes the calculated corner magnitude (Bird et al., 2002). Dashed curves in d show the calculated M_w dependence on A_t with slip (S) of 60 cm and 0.5 cm.

and seismogenic area of the transform faults. The maximum moment magnitude decreases with increasing spreading rate, reflecting relatively small age offset and seismogenic area of fast-spreading systems, as well as the presence of lizardite mineral phases in slow-spreading systems that might promote unstable transform sliding.

Acknowledgements

This work benefited from constructive discussion with Jason Phipps Morgan, Marcia Maia, Hongfeng Yang, Zhiyuan Zhou, and the Deep Ocean Geodynamics Group of the South China Sea Institute of Oceanology.

References

Baines A G, Cheadle M J, Dick H J B, et al. 2003. Mechanism for generating the anomalous uplift of oceanic core complexes: Atlantis Bank, Southwest Indian Ridge. Geology, 31(12): 1105–1108, doi: 10.1130/G19829.1

Behn M D, Lin J, Zuber M T. 2002. Evidence for weak oceanic transform faults. Geophysical Research Letters, 29(24): 2207, doi: 10.1029/2002GL015612

Bird P, Kagan Y Y, Jackson D D. 2002. Plate tectonics and earthquake potential of spreading ridges and oceanic transform faults. In: Stein S, Freymueller J T, eds. Plate Boundary Zones. Washington, DC: Geodynamics Series, 203–218

Boettcher M S, Jordan T H. 2004. Earthquake scaling relations for mid-ocean ridge transform faults. Journal of Geophysical Research: Solid Earth, 109(B12): B12302, doi: 10.1029/2004JB003110

Bonatti E, Ligi M, Gasperini L, et al. 1994. Transform migration and vertical tectonics at the Romanche fracture zone, equatorial Atlantic. Journal of Geophysical Research: Solid Earth, 99(B11): 21779–21802, doi: 10.1029/94JB01178

Chen Y S, Morgan W J. 1990. Rift valley/no rift valley transition at mid-ocean ridges. Journal of Geophysical Research: Solid Earth, 95(B11): 17571–17581, doi: 10.1029/JB095iB11p17571

Croon M B, Cande S C, Stock J M. 2008. Revised pacific-Antarctic plate motions and geophysics of the Menard fracture zone. Geochemistry, Geophysics, Geosystems, 9(7): Q07001, doi: 10.1029/2008GC002019

Dick H, Lin J, Schouten H. 2003. An ultraslow-spreading class of ocean ridge. Nature, 426(6965): 405–412, doi: 10.1038/nature02128

Dziewonski A M, Anderson D L. 1981. Preliminary reference Earth model. Physics of the Earth and Planetary Interiors, 25(4): 297–356, doi: 10.1016/0031-9201(81)90046-7

Ekström G, Nettles M, Dziewoński A M. 2012. The global CMT project 2004–2010 : Centroid-moment tensors for 13, 017 earthquakes. Physics of the Earth and Planetary Interiors, 200–201: 1–9, doi:

10.1016/j.pepi.2012.04.002
Embley R W, Wilson D S. 1992. Morphology of the Blanco transform fault zone-NE Pacific: implications for its tectonic evolution. Marine Geophysical Researches, 14(1): 25–45, doi: 10.1007/BF01674064
Fornari D J, Gallo D G, Edwards M H, et al. 1989. Structure and topography of the Siqueiros transform fault system: Evidence for the development of intra-transform spreading centers. Marine Geophysical Researches, 11(4): 263–299, doi: 10.1007/BF00282579
Fox P J, Gallo D G. 1984. A tectonic model for ridge-transform-ridge plate boundaries: Implications for the structure of oceanic lithosphere. Tectonophysics, 104(3–4): 205–242, doi: 10.1016/0040-1951(84)90124-0
Georgen J E, Lin J, Dick H J B. 2001. Evidence from gravity anomalies for interactions of the Marion and Bouvet hotspots with the Southwest Indian Ridge: Effects of transform offsets. Earth and Planetary Science Letters, 187(3–4): 283–300, doi: 10.1016/S0012-821X(01)00293-X
Gregg P M, Lin J, Smith D K. 2006. Segmentation of transform systems on the East Pacific Rise: Implications for earthquake processes at fast-slipping oceanic transform faults. Geology, 34(4): 289–292, doi: 10.1130/G22212.1
Gregg P M, Lin J, Behn M D, et al. 2007. Spreading rate dependence of gravity anomalies along oceanic transform faults. Nature, 448(7150): 183–187, doi: 10.1038/nature05962
Kanamori H. 1977. The energy release in great earthquakes. Journal of Geophysical Research, 82(20): 2981–2987, doi: 10.1029/JB082i020p02981
Karson J A, Dick H J B. 1983. Tectonics of ridge-transform intersections at the Kane fracture zone. Marine Geophysical Research, 6(1): 51–98, doi: 10.1007/BF00300398
Kreemer C, Haines J, Holt W E, et al. 2000. On the determination of a global strain rate model. Earth, Planets and Space, 52(10): 765–770, doi: 10.1186/BF03352279
Ligi M, Bonatti E, Gasperini L, et al. 2002. Oceanic broad multifault transform plate boundaries. Geology, 30(1): 11–14, doi: 10.1130/0091-7613(2002)030<0011:OBMTPB>2.0.CO;2
Lin J, Parmentier E M. 1989. Mechanisms of lithospheric extension at mid-ocean ridges. Geophysical Journal International, 96(1): 1–22, doi: 10.1111/j.1365-246X.1989.tb05246.x
Lin J, Purdy G M, Schouten H, et al. 1990. Evidence from gravity data for focusedmagmatic accretion along the Mid-Atlantic Ridge. Nature, 344: 627–632, doi: 10.1038/344627a0
Lin J, Morgan J P. 1992. The spreading rate dependence of three-dimensional mid-ocean ridge gravity structure. Geophysical Research Letters, 19(1): 13–16, doi: 10.1029/91GL03041
Livermore R A, Tomlinson J S, Woollett R W. 1991. Unusual sea-floor fabric near the Bullard fracture zone imaged by GLORIA sidescan sonar. Nature, 353(6340): 158–161, doi: 10.1038/353158a0
Lonsdale P. 1994. Structural geomorphology of the Eltanin fault system and adjacent transform faults of the Pacific-Antarctic plate boundary. Marine Geophysical Researches, 16(2): 105–143, doi: 10.1007/BF01224756
Macdonald K C. 1982. Mid-ocean ridges: Fine scale tectonic, volcanic and hydrothermal processes within the plate boundary zone. Annual Review of Earth and Planetary Sciences, 10: 155–190, doi: 10.1146/annurev.ea.10.050182.001103
Magde L S, Detrick R S. 1995. Crustal and upper mantle contribution to the axial gravity anomaly at the southern East Pacific Rise. Journal of Geophysical Research: Solid Earth, 100(B3): 3747–3766, doi: 10.1029/94JB02869
Maia M. 2019. Topographic and morphologic evidences of deformation at oceanic transform faults: Far-field and local-field stresses. In: Duarte J C, ed. Transform Plate Boundaries and Fracture Zones. Amsterdam: Elsevier, 61–87, doi: 10.1016/B978-0-12-812064-4.00003-7
Morgan J P, Parmentier E M. 1984. Lithospheric stress near a ridge-transform intersection. Geophysical Research Letters, 11(2): 113–116, doi: 10.1029/GL011i002p00113
Perfit M R, Fornari D J, Ridley W I, et al. 1996. Recent volcanism in the Siqueiros transform fault: Picritic basalts and implications for MORB magma genesis. Earth and Planetary Science Letters, 141(1–4): 91–108, doi: 10.1016/0012-821X(96)00052-0
Pockalny R A, Detrick R S, Fox P J. 1988. Morphology and tectonics of the Kane transform from Sea Beam bathymetry data. Journal of Geophysical Research: Solid Earth, 93(B4): 3179–3193, doi: 10.1029/JB093iB04p03179
Pockalny R A, Fox P J, Fornari D J, et al. 1997. Tectonic reconstruction of the Clipperton and Siqueiros Fracture Zones: Evidence and consequences of plate motion change for the last 3 Myr. Journal of Geophysical Research: Solid Earth, 102(B2): 3167–3181, doi: 10.1029/96JB03391
Roland E, Behn M D, Hirth G. 2010. Thermal-mechanical behavior of oceanic transform faults: Implications for the spatial distribution of seismicity. Geochemistry, Geophysics, Geosystems, 11(7): Q07001, doi: 10.1029/2010GC003034
Royden L H, Horváth F, Burchfiel B C. 1982. Transform faulting, extension, and subduction in the Carpathian Pannonian region. GSA Bulletin, 93(8): 717–725, doi: 10.1130/0016-7606(1982)93<717:TFEASI>2.0.CO;2
Sandwell D T, Müller R D, Smith W H F, et al. 2014. New global marine gravity model from CryoSat-2 and Jason-1 reveals buried tectonic structure. Science, 346(6205): 65–67, doi: 10.1126/science.1258213
Sclater J G, Grindlay N R, Madsen J A, et al. 2005. Tectonic interpretation of the Andrew Bain transform fault: Southwest Indian Ocean. Geochemistry, Geophysics, Geosystems, 6(9): Q09K10, doi: 10.1029/2005GC000951
Searle R C. 1983. Multiple, closely spaced transform faults in fast-slipping fracture zones. Geology, 11(10): 607–610, doi: 10.1130/0091-7613(1983)11<607:MCSTFI>2.0.CO;2
Searle R C, Thomas M V, Jones E J W. 1994. Morphology and tectonics of the Romanche Transform and its environs. Marine Geophysical Researches, 16(6): 427–453, doi: 10.1007/bf01270518
Sempéré J C, Lin J, Brown H S, et al. 1993. Segmentation and morphotectonic variations along a slow-spreading center: The Mid-Atlantic Ridge (24°00′N–30°40′N). Marine Geophysical Researches, 15(3): 153–200, doi: 10.1007/BF01204232
Shaw W J, Lin J. 1996. Models of ocean ridge lithospheric deformation: Dependence on crustal thickness, spreading rate, and segmentation. Journal of Geophysical Research: Solid Earth, 101(B8): 17977–17993, doi: 10.1029/96JB00949
Sleep N H. 1969. Sensitivity of heat flow and gravity to the mechanism of sea-floor spreading. Journal of Geophysical Research, 74(2): 542–549, doi: 10.1029/JB074i002p00542
Sleep N H, Biehler S. 1970. Topography and tectonics at the intersections of fracture zones with central rifts. Journal of Geophysical Research, 75(14): 2748–2752, doi: 10.1029/JB075i014p02748
Tapponnier P, Francheteau J. 1978. Necking of the lithosphere and the mechanics of slowly accreting plate boundaries. Journal of Geophysical Research: Solid Earth, 83(B8): 3955–3970, doi: 10.1029/JB083iB08p03955
Tozer B, Sandwell D T, Smith W H F, et al. 2019. Global bathymetry and topography at 15 arc sec: SRTM15+. Earth and Space Science, 6(10): 1847–1864, doi: 10.1029/2019EA000658
Tucholke B E, Lin J. 1994. A geological model for the structure of ridge segments in slow spreading ocean crust. Journal of Geophysical Research: Solid Earth, 99(B6): 11937–11958, doi: 10.1029/94JB00338
Tucholke B E, Schouten H. 1988. Kane fracture zone. Marine Geophysical Researches, 10(1–2): 1–39, doi: 10.1007/BF02424659
Turcotte D L, Schubert G. 2014. Geodynamics. 3rd ed. Cambridge, United Kingdom: Cambridge University Press, 636
Wei M. 2019. Seismic behavior on oceanic transform faults at the East Pacific Rise. In Duarte J C, ed. Transform Plate Boundaries and Fracture Zones. Amsterdam: Elsevier, 119–143, doi: 10.1016/B978-0-12-812064-4.00006-2
Wilson J T. 1965. A new class of faults and their bearing on continental drift. Nature, 207(4995): 343–347, doi: 10.1038/207343a0
Wolfson-Schwehr M. 2015. The relationship between oceanic transform fault segmentation, seismicity, and thermal structure [dissertation]. Durham: University of New Hampshire, https://scholars.unh.edu/dissertation/2233
Wolfson-Schwehr M, Boettcher M S. 2019. Global characteristics of oceanic transform fault structure and seismicity. In: Duarte J C, ed. Transform Plate Boundaries and Fracture Zones. Amsterdam: Elsevier, 21–59, doi: 10.1016/B978-0-12-812064-4.00002-5
Zhang Tao, Lin Jian, Gao Jinyao. 2020. Asymmetric crustal structure of the ultraslow-spreading Mohns Ridge. International Geology Review, 62(5): 568–584, doi: 10.1080/00206814.2019.1627586

Appendix:

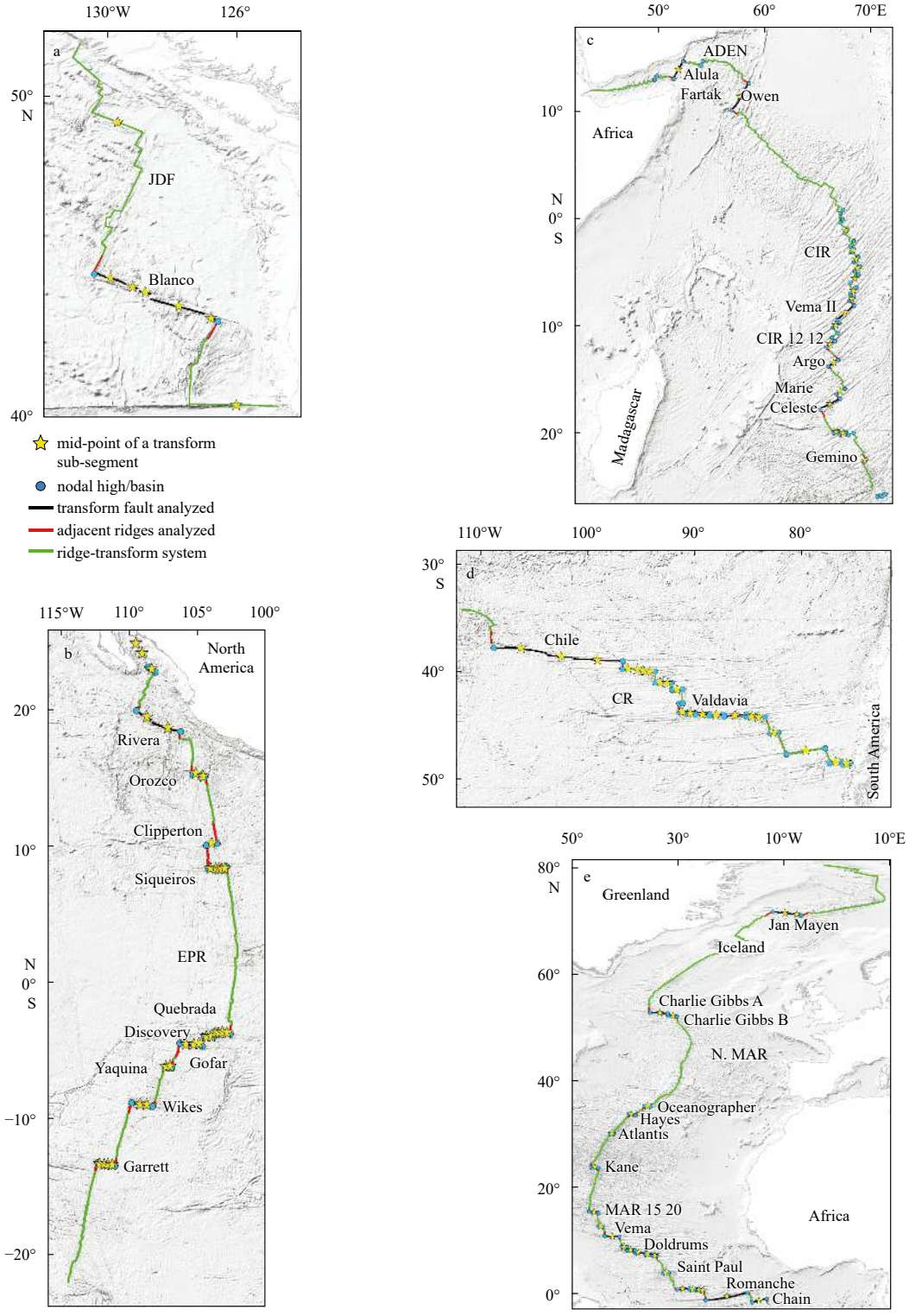

Fig. A1.

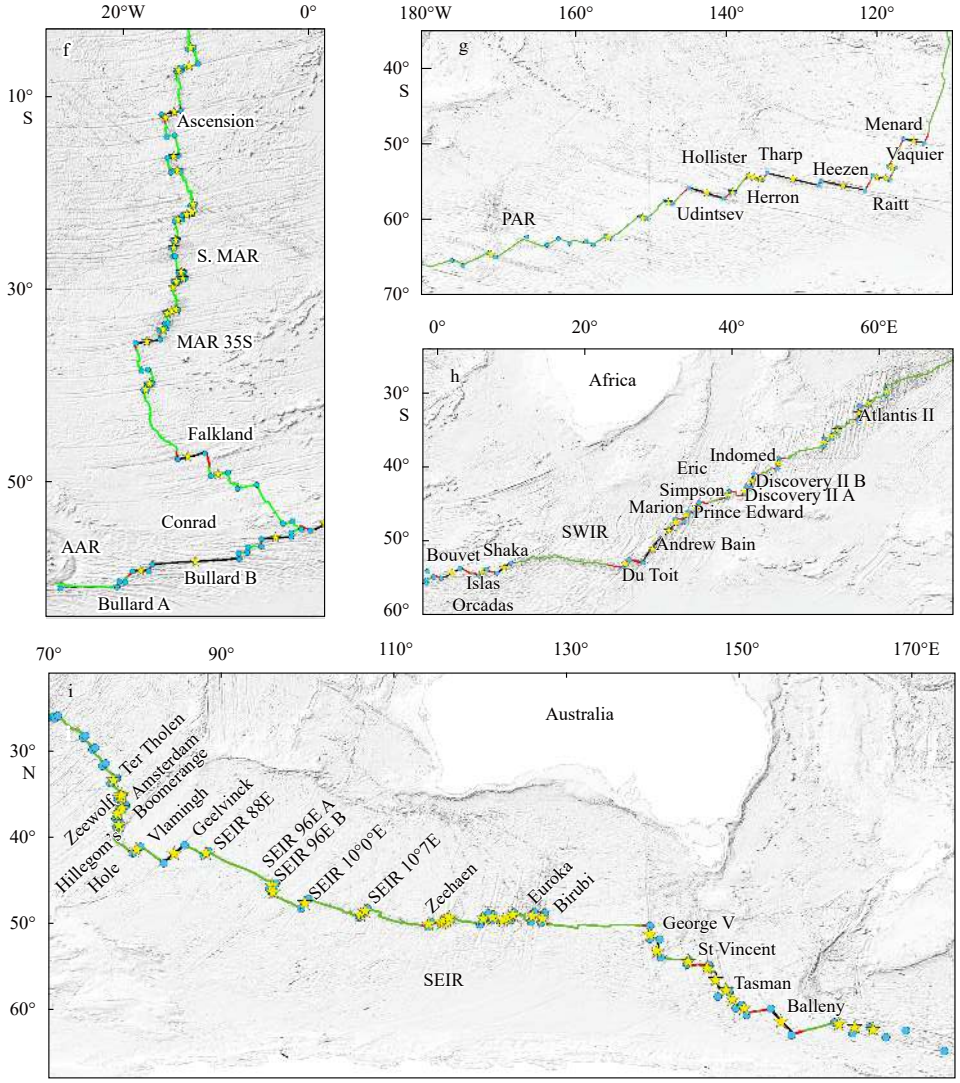

Fig. A1. Topography maps of tectonic regions studied. a. JDF: Juan de Fuca Ridge; b. EPR: East Pacific Rise; c. ADEN-CIR: Aden Ridge-Central Indian Ridge; d. CR: Chile Rise; e. N. MAR: North Mid-Atlantic Ridge; f. S. MAR: South Mid-Atlantic Ridge; g. PAR: Pacific-Antarctic Ridge; h. SWIR: Southwest Indian Ridge; and i. SEIR: Southeast Indian Ridge. Yellow stars: mid-point of a transform sub-segment analyzed for length. Black lines: transform depth analyzed. Red lines: adjacent ridges depth analyzed. Green lines: along ridge-transform profiles from the global bathymetry dataset; Blue dots: ridge-transform intersections.

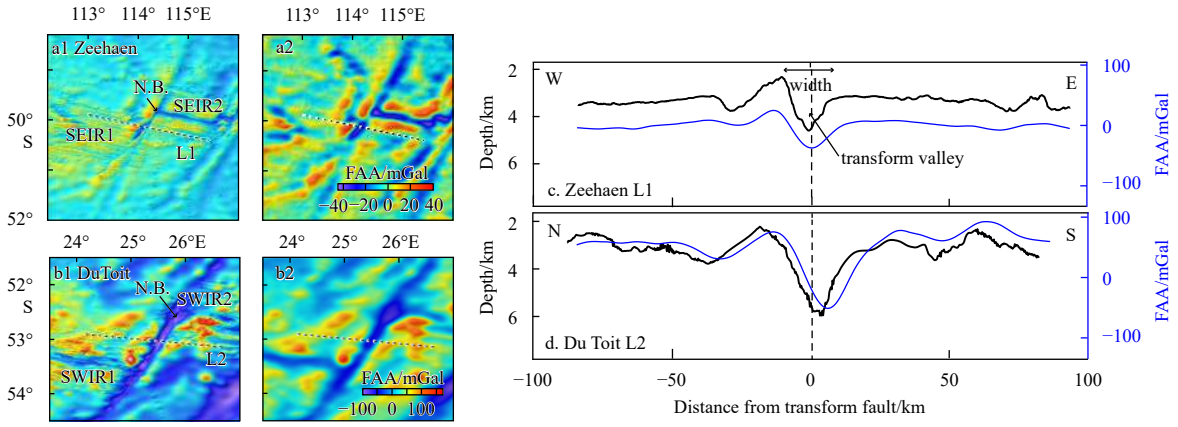

Fig. A2. Examples of transform faults. a1. Seafloor depth and a2. FAA of the Zeehaen transform fault, as an example of an intermediate-spreading ridge; b1. Seafloor depth and b2. FAA of the Du Toit transform fault, as an example of an ultraslow-spreading ridge; c and d. profiles of seafloor topography (black) and FAA (blue) across the Zeehaen and Du Toit transform faults. Dashed lines (L1, L2) denote locations of across-transform profiles. N.B.: nodal basin; SEIR: Southeast Indian Ridge.

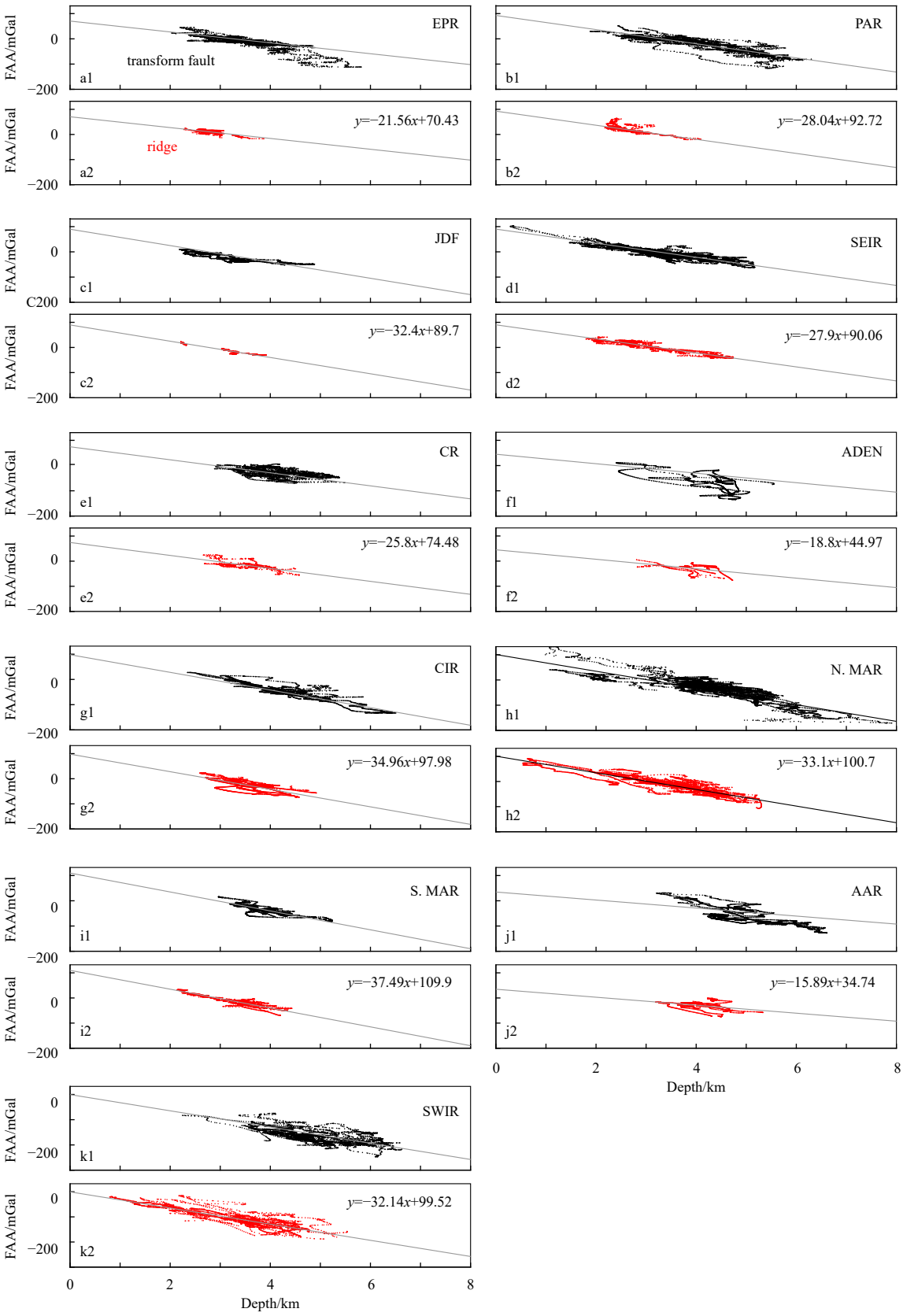

Fig. A3. Correlation between FAA and depth of the analyzed transform faults (black) and adjacent ridges (red). Multiple regions: a. EPR: East Pacific Rise; b. PAR: Pacific-Antarctic Ridge; c. JDF: Juan de Fuca Ridge; d. SEIR: Southeast Indian Ridge; e. CR: Chile Rise; f. ADEN: Aden Ridge; g. CIR: Central Indian Ridge; h. N. MAR: North Mid-Atlantic Ridge; i. S. MAR: South Mid-Atlantic Ridge; j. AAR: American-Antarctic Ridge; k. SWIR: Southwest Indian Ridge. Grey lines represent the best-fitting lines of the ridge values for each region.

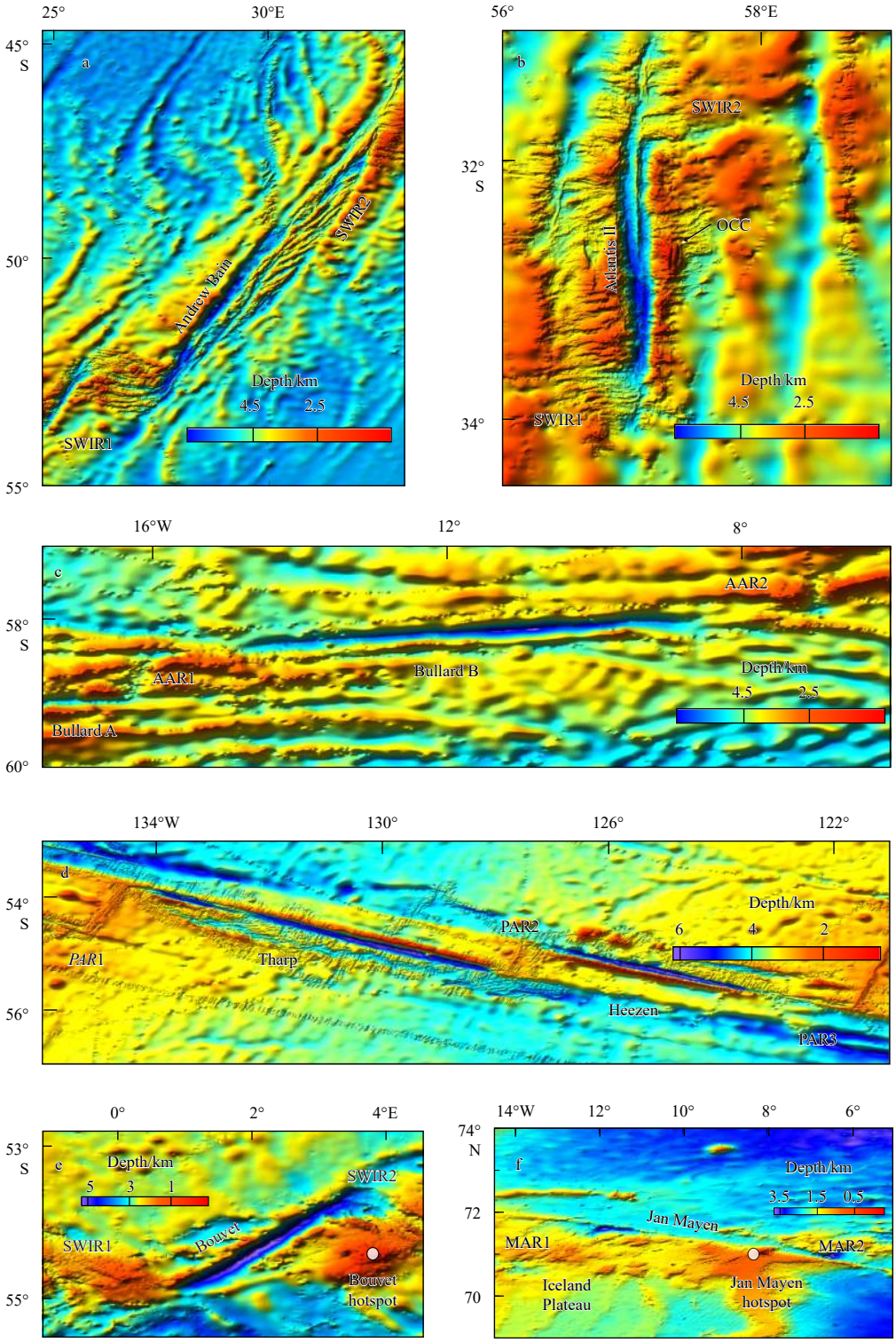

Fig. A4. Maps of the transform systems with major morphological anomalies: Andrew Bain (a), Atlantis II (b), Bullard (c), Heezen and Tharp (d), Bouvet (e), and Jan Mayen (f). OCC: Oceanic core complex; SWIR: Southwest Indian Ridge; AAR: American-Antarctic Ridge; PAR: Pacific-Antarctic Ridge; MAR: Mid-Atlantic Ridge.

Table A1. Compilation of global oceanic transform faults with a total of 201 individual fault segments[1)]

No.	Name	Segment mid-point		Length/km	Full rate/ (mm·a^{-1})	Age offset/Ma	M_w^{max}	A_t/km^2
		Latitude	Longitude					
1	Alula Fartak	13.94°N	51.71°E	203	18.90	21.48	6.6	2 724
2	Amsterdam	36.70°S	78.69°E	108	62.02	3.48	6.2	584
3	Andrew Bain A	47.49°S	32.23°E	87	13.35	13.03	6.4	909
4	Andrew Bain B	48.55°S	31.30°E	148	13.34	22.19	6.4	2018
5	Andrew Bain C	51.00°S	29.07°E	471	13.33	70.67	6.4	11 464
6	Argo	13.59°S	66.35°E	102	33.33	6.12	6.0	731
7	Ascension A	7.37°S	13.25°W	58	29.54	3.93	5.6	333
8	Ascension B	6.88°S	12.14°W	203	29.51	13.76	6.0	2 180
9	Atlantis	30.06°N	42.35°W	63	22.40	5.63	5.8	432
10	Atlantis II	32.76°S	57.04°E	201	12.02	33.44	5.8	3 365
11	Balleny	61.43°S	154.81°E	350	64.50	10.85	6.7	3 340
12	Birubi	49.50°S	127.26°E	148	69.62	4.25	5.4	884
13	Blanco A	44.33°N	129.92°W	94	51.06	3.68	6.2	523
14	Blanco B	44.05°N	129.23°W	24	51.01	0.94	6.2	67
15	Blanco C	43.89°N	128.84°W	41	50.99	1.61	5.4	150
16	Blanco D	43.45°N	127.81°W	135	50.94	5.30	6.4	900
17	Blanco E	43.08°N	126.83°W	41	50.93	1.61	6.4	151
18	Bode Verde A	12.25°S	14.59°W	56	30.02	3.73	4.9	313
19	Bode Verde B	11.68°S	13.70°W	162	29.98	10.81	6.2	1 542
20	Boomerang	37.36°S	78.21°E	35	62.15	1.13	5.8	108
21	Bouvet	54.26°S	1.92°E	201	12.72	31.60	6.6	3 271
22	Bullard A	59.13°S	17.14°W	95	12.99	14.63	6.2	1 051
23	Bullard B	58.18°S	11.49°W	526	13.43	78.33	6.8	13 479
24	Chain	1.24°S	14.52°W	313	28.58	21.9	6.8	4 242
25	Challenger A	37.00°S	96.62°W	78	46.56	3.35	5.8	414
26	Challenger B	37.11°S	95.72°W	67	46.58	2.88	–	329
27	Challenger C	37.25°S	95.19°W	20	46.61	0.86	–	53
28	Challenger D	37.32°S	94.58°W	82	46.62	3.52	5.4	446
29	Charlie Gibbs A	52.62°N	33.26°W	203	21.73	18.68	7.1	2 541
30	Charlie Gibbs B	52.12°N	30.82°W	110	21.83	10.08	5.8	1 011
31	Chile 38S A	38.33°S	93.63°W	43	46.85	1.84	5.3	169
32	Chile 38S B	38.41°S	92.98°W	68	46.86	2.90	–	336
33	Chile 39S	38.96°S	92.07°W	84	46.98	3.58	6.1	460
34	Chile A	35.14°S	106.51°W	493	46.42	21.24	6.3	6 580
35	Chile B	35.90°S	102.79°W	186	46.46	8.01	6.7	1 525
36	Chile C	36.21°S	99.42°W	420	46.43	18.09	6.5	5 174
37	Chiloe	43.03°S	83.08°W	61	47.82	2.55	5.6	282
38	CIR 10S	10.09°S	66.56°E	76	30.95	4.91	5.0	488
39	CIR 12 12	11.85°S	65.99°E	106	31.90	6.65	5.7	791
40	CIR 16S	16.29°S	66.97°E	110	35.58	6.18	5.6	792
41	CIR 1S	1.19°S	67.52°E	50	29.87	3.35	5.8	265
42	CIR 5S	4.73°S	68.59°E	49	31.00	3.16	5.3	252
43	CIR 6S	6.83°S	68.24°E	89	31.35	5.68	5.4	614
44	CIR 7S	7.61°S	68.08°E	62	30.17	4.11	5.4	364
45	Clipperton	10.22°N	103.95°W	84	106.28	1.58	6.6	307
46	Conrad	55.71°S	3.16°W	198	14.51	27.29	6.7	2 995
47	Darwin	45.90°S	76.36°W	53	48.30	2.19	5.9	227
48	Discovery A	4.01°S	104.35°W	36	123.55	0.58	6.0	80
49	Discovery B	4.00°S	104.01°W	27	123.48	0.44	5.8	52
50	Discovery II A	43.30°S	41.66°E	124	12.91	19.21	6.4	1 573
51	Discovery II B	41.86°S	42.59°E	216	12.89	33.51	6.7	3 620
52	Doldrums A	8.82°N	40.02°W	109	25.56	8.53	5.6	922
53	Doldrums B	8.21°N	38.78°W	162	25.74	12.59	7.0	1 664
54	Doldrums C	7.72°N	37.38°W	149	25.89	11.51	6.2	1 464
55	Doldrums D	7.40°N	35.66°W	229	26.00	17.62	6.5	2 783

to be continued

Continued from Table A1

No.	Name	Segment mid-point		Length/km	Full rate/ (mm·a^{-1})	Age offset/Ma	M_w^{max}	A_t/km^2
		Latitude	Longitude					
56	Doldrums E	7.19°N	34.28°W	77	26.08	5.90	5.9	542
57	Du Toit	53.01°S	25.48°E	130	13.29	19.56	6.2	1 664
58	Egeria	20.13°S	66.58°E	46	38.13	2.41	5.5	207
59	Eric Simpson	43.73°S	39.25°E	89	13.03	13.66	6.7	952
60	Euroka	49.23°S	126.10°E	134	69.76	3.84	5.6	761
61	Falkland	47.31°S	12.25°W	181	27.44	13.19	6.0	1904
62	Flinders	20.24°S	67.26°E	65	38.48	3.38	5.2	346
63	Gallieni	36.64°S	52.32°E	114	12.34	18.48	6.9	1 418
64	Garrett A	13.41°S	112.15°W	39	133.99	0.58	5.9	87
65	Garrett B	13.42°S	111.80°W	26	133.94	0.39	5.2	47
66	Garrett C	13.449°S	111.525°W	32	133.90	0.48	5.7	–
67	Garrett D	13.476°S	111.242°W	27	133.86	0.40	5.8	–
68	Gauss	35.00°S	54.12°E	59	12.23	9.65	6.2	530
69	Gazelle	35.80°S	53.43°E	81	12.27	13.20	5.8	852
70	Geelvinck	41.96°S	84.71°E	303	65.60	9.24	5.5	2 668
71	Gemino	22.78°S	69.29°E	38	40.99	1.85	5.4	150
72	George V A	51.35°S	139.72°E	235	67.49	6.96	6.5	1 797
73	George V B	53.24°S	140.55°E	179	67.30	5.32	5.8	1 196
74	GoC 24N	24.24°N	109.05°W	61	50.37	2.42	6.1	885
75	GoC 25N	24.98°N	109.52°W	119	49.85	4.77	6.7	753
76	Gofar A	4.59°S	105.85°W	95	124.55	1.53	6.2	341
77	Gofar B	4.58°S	105.26°W	29	124.40	0.47	6.0	58
78	Gofar C	4.56°S	104.88°W	46	124.30	0.74	6.1	115
79	Gough	39.79°S	16.23°W	56	28.98	3.86	4.9	319
80	Guafo	44.70°S	80.15°W	286	48.10	11.89	6.4	2 857
81	Guamblin	45.71°S	77.37°W	80	48.27	3.31	6.0	422
82	Hayes	33.66°N	38.65°W	80	21.65	7.39	6.1	629
83	Heemskerck A	50.01°S	115.58°E	19	70.34	0.54	–	40
84	Heemskerck B	49.88°S	115.93°E	24	70.34	0.68	–	57
85	Heemskerck C	49.65°S	116.19°E	27	70.34	0.77	–	68
86	Heemskerck D	49.40°S	116.47°E	31	70.33	0.88	–	84
87	Heezen	55.42°S	124.53°W	382	79.02	9.67	6.4	3 441
88	Herron	56.29°S	139.07°W	26	75.45	0.69	5.9	63
89	Hillegom's Hole	38.66°S	78.31°E	59	62.70	1.88	6.4	235
90	Hollister A	54.22°S	136.90°W	23	77.89	0.59	6.3	51
91	Hollister B	54.35°S	136.23°W	62	77.93	1.59	6.4	227
92	Hollister C	54.53°S	135.39°W	34	77.95	0.87	6.1	92
93	Indomed	39.47°S	46.11°E	141	12.73	22.15	5.8	1921
94	Islas Orcadas	54.18°S	6.10°E	100	12.85	15.56	6.1	1 142
95	Jan Mayen A	71.37°S	9.64°W	127	15.45	16.44	6.7	1 491
96	Jan Mayen B	71.14°N	7.39°W	27	15.45	3.50	6.7	145
97	Kane	23.74°N	45.62°W	146	23.43	12.46	6.4	1 492
98	L'Astronome	59.65°S	150.85°W	56	68.94	1.62	6.0	207
99	Le Geographe	57.63°S	147.50°W	70	71.90	1.95	5.9	283
100	Mabahiss	3.04°S	68.12°E	42	30.48	2.76	5.6	202
101	MAR 15 20	15.28°N	45.74°W	193	23.57	16.38	6.0	2 262
102	MAR 18S	17.72°S	13.37°W	91	30.34	6.00	5.5	645
103	MAR 21S	21.23°S	11.72°W	45	30.40	2.96	–	224
104	MAR 22S A	22.82°S	13.26°W	85	30.39	5.59	5.4	582
105	MAR 22S B	22.28°S	12.37°W	86	30.40	5.66	5.2	592
106	MAR 22S C	22.02°S	11.83°W	22	30.40	1.45	5.2	76
107	MAR 25 50S	25.66°S	13.74°W	39	30.32	2.57	5.5	181
108	MAR 25S	24.90°S	13.55°W	37	30.35	2.44	5.4	167
109	MAR 29 45S	29.76°S	13.77°W	27	30.10	1.79	–	104
110	MAR 29S A	29.19°S	13.45°W	74	30.13	4.91	5.0	475

to be continued

Continued from Table A1

No.	Name	Segment mid-point		Length/km	Full rate/ (mm·a^{-1})	Age offset/Ma	M_w^{max}	A_t/km^2
		Latitude	Longitude					
111	MAR 29S B	28.87°S	12.77°W	59	30.15	3.91	5.2	338
112	MAR 32S A	32.50°S	14.42°W	23	29.87	1.54	–	82
113	MAR 32S B	32.27°S	13.95°W	57	29.89	3.81	5.3	322
114	MAR 32S C	32.11°S	13.48°W	29	29.90	1.94	5.9	117
115	MAR 34S	34.16°S	14.83°W	69	29.71	4.64	5.2	431
116	MAR 35S	35.40°S	16.51°W	250	29.60	16.89	6.9	2 975
117	MAR 40S	40.35°S	16.64°W	40	28.90	2.77	–	192
118	MAR 50S	49.13°S	9.14°W	110	26.90	8.18	5.4	911
119	MAR 5S	5.04°S	11.94°W	78	29.27	5.33	5.6	521
120	Marathon	12.64°N	44.46°W	88	24.41	7.21	5.5	684
121	Marie Celeste	17.51°S	66.00°E	219	35.99	12.17	6.6	2 213
122	Marion	46.47°S	33.66°E	109	13.22	16.49	6.2	1 281
123	Melville	29.84°S	60.78°E	92	11.74	15.67	6.9	1 054
124	Menard	49.56°S	115.24°W	208	85.47	4.87	6.4	1 330
125	Mendocino	40.373 5°N	126.039°W	237	49.48	9.58	–	–
126	Novara	31.43°S	58.41°E	45	11.93	7.54	–	362
127	Oceanographer	35.18°N	35.64°W	121	21.27	11.38	6.3	1 182
128	Orozco A	15.41°N	105.11°W	46	87.81	1.05	5.3	137
129	Orozco B	15.16°N	104.58°W	23	88.85	0.52	5.6	48
130	Owen	11.42°N	57.54°E	335	22.84	29.33	6.5	5 254
131	PAR 161	61.78°S	161.50°E	77	45.98	3.35	6.0	408
132	PAR 163	62.10°S	163.36°E	85	46.71	3.64	5.3	470
133	PAR 165	62.38°S	165.46°E	89	47.58	3.74	5.9	499
134	Pitman	64.53°S	170.78°W	71	56.74	2.50	5.3	325
135	Prince Edward	45.45°S	35.13°E	146	13.19	22.14	6.4	1989
136	Quebrada A	3.74°S	103.68°W	27	123.12	0.44	5.6	52
137	Quebrada B	3.73°S	103.44°W	22	123.05	0.36	5.3	38
138	Quebrada C	3.70°S	103.189°W	27	122.97	0.44	4.9	52
139	Quebrada D	3.73°S	102.86°W	42	122.94	0.68	5.6	–
140	Raitt A	54.33°S	120.10°W	88	80.94	2.17	5.4	376
141	Raitt B	54.49°S	118.94°W	58	80.99	1.43	6.0	201
142	Rio Grande	28.23°S	12.94°W	57	30.19	3.78	5.2	321
143	Rivera A	19.57°N	108.68°W	177	73.00	4.85	6.3	1 130
144	Rivera B	18.76°N	107.16°W	197	73.00	5.40	6.9	1 326
145	Romanche	0.53°S	20.63°W	878	28.27	62.12	7.1	20 036
146	Saint Exupery	62.24°S	155.42°W	42	64.73	1.30	5.7	139
147	Saint Paul A	0.93°N	29.02°W	297	27.71	21.44	6.6	3 982
148	Saint Paul B	0.87°N	27.04°W	146	27.77	10.51	5.9	1 371
149	Saint Paul C	0.74°N	25.92°W	96	27.83	6.90	6.1	730
150	Saint Paul D	0.62°N	25.23°W	50	27.88	3.59	6.0	274
151	Sealark	3.88°S	68.47°E	63	30.78	4.09	5.1	369
152	SEIR 100E	47.68°S	99.81°E	129	69.46	3.71	6.5	721
153	SEIR 106E A	49.09°S	106.26°E	56	70.11	1.60	5.0	205
154	SEIR 106E B	48.64°S	106.79°E	59	70.12	1.68	5.5	222
155	SEIR 120	49.49°S	120.42°E	154	70.19	4.39	5.3	935
156	SEIR 121	49.36°S	121.53°E	80	70.13	2.28	5.3	350
157	SEIR 122	49.71°S	122.73°E	50	70.04	1.43	5.3	173
158	SEIR 88E	41.92°S	88.42°E	65	66.47	1.96	5.8	264
159	SEIR 96E A	45.66°S	96.03°E	89	68.69	2.59	6.4	415
160	SEIR 96E B	46.43°S	96.14°E	40	68.82	1.16	5.7	125
161	Shackelton	59.77°S	59.12°W	332	6.83	97.22	6.6	9 477
162	Shaka	53.55°S	9.02°E	199	12.92	30.80	6.8	3 198
163	Siqueiros A	8.40°N	104.05°W	24	112.24	0.43	5.5	46
164	Siqueiros B	8.38°N	103.66°W	34	112.48	0.60	5.6	77
165	Siqueiros C	8.36°N	103.42°W	18	112.68	0.32	5.8	30

to be continued

Continued from Table A1

No.	Name	Segment mid-point		Length/km	Full rate/(mm·a^{-1})	Age offset/Ma	M_w^{max}	A_t/km^2
		Latitude	Longitude					
166	Siqueiros D	8.36°N	103.21°W	17	112.89	0.30	5.8	27
167	Siqueiros E	8.38°N	103.00°W	17	112.96	0.30	5.9	27
168	Sovanco	48.98°N	129.77°W	135	53.90	5.01	6.7	875
169	St Vincent	54.50°S	144.12°E	58	66.50	1.74	5.9	222
170	Strakhov	3.94°N	32.08°W	108	26.96	8.01	5.5	885
171	Tasman A	55.23°S	146.33°E	90	66.05	2.73	6.9	431
172	Tasman B	56.59°S	147.28°E	218	65.82	6.62	6.4	1 626
173	Tasman C	57.80°S	148.47°E	62	65.51	1.89	6.5	247
174	Tasman D	58.87°S	149.25°E	173	65.29	5.30	6.3	1 154
175	Tasman E	59.89°S	150.57°E	82	65.29	2.51	6.5	377
176	Ter Tholen	33.44°S	77.72°E	89	60.26	2.95	5.3	443
177	Tetyaev	16.25°S	13.75°W	123	30.28	8.12	5.5	1 015
178	Tharp	54.59°S	131.12°W	462	78.82	11.72	6.6	4 582
179	Tomayo	23.08°N	108.34°W	65	50.95	2.55	6.5	301
180	Udintsev	56.41°S	142.43°W	325	74.49	8.73	6.4	2 781
181	Vacquier	53.04°S	118.09°W	52	82.29	1.26	5.8	170
182	Valdavia A	41.09°S	91.56°W	49	47.42	2.07	5.4	204
183	Valdavia B	41.20°S	90.81°W	77	47.45	3.25	5.8	402
184	Valdavia C	41.30°S	89.74°W	97	47.47	4.09	5.7	568
185	Valdavia D	41.35°S	88.44°W	119	47.48	5.01	5.7	772
186	Valdavia E	41.41°S	86.72°W	165	47.51	6.95	5.9	1 260
187	Valdavia F	41.49°S	85.14°W	69	47.54	2.90	5.6	340
188	Valdavia G	41.57°S	84.52°W	23	47.56	0.97	–	65
189	Vema	10.78°N	42.29°W	307	24.98	24.58	6.9	4 407
190	Vema II	8.92°S	67.44°E	237	30.63	15.48	6.2	2 700
191	Vityaz	5.69°S	68.37°E	105	31.14	6.74	5.7	790
192	Vlamingh	41.47°S	80.36°E	123	64.35	3.82	6.4	697
193	Warringa A	49.41°S	123.38°E	38	70.00	1.09	5.3	115
194	Warringa B	49.07°S	123.87°E	49	69.97	1.40	–	168
195	Wilkes A	9.02°S	109.21°W	35	129.79	0.54	5.9	75
196	Wilkes B	9.06°S	108.69°W	74	129.74	1.14	6.1	230
197	Yaquina A	6.25°S	107.31°W	23	126.66	0.36	5.6	40
198	Yaquina B	6.18°S	106.99°W	21	126.51	0.33	5.2	35
199	Zeehaen	50.12°S	114.12°E	71	70.35	2.02	5.6	292
200	Zeewolf A	35.44°S	78.46°E	32	61.41	1.04	5.0	95
201	Zeewolf B	35.18°S	78.64°E	29	61.36	0.95	5.3	82

Notes: [1)] Data are from Wolfson-Schwehr (2015) and Wolfson-Schwehr & Boettcher (2019). – means no earthquakes recorded by the International Seismic Network or no estimate of A_t provided by Wolfson-Schwehr (2015) and Wolfson-Schwehr and Boettcher (2019).

Table A2. Depth of 78 ridge-transform fault systems

No.[1)]	Name	D_T/km	STD of D_T/km	D_R/km	D_{R1}/km	STD of D_{R1}/km	D_{R2}/km	STD of D_{R2}/km	D_T–D_R/km	STD of (D_T–D_R)/km
1	Alula Fartak	3.90	0.77	3.56	3.49	0.46	3.63	0.34	0.34	1.17
2	Amsterdam	2.97	0.54	2.41	2.07	0.08	2.76	0.08	0.56	0.62
3–5	Andrew Bain	5.54	0.73	3.71	4.32	0.48	3.10	0.63	1.83	1.28
6	Argo	4.09	0.47	3.39	3.04	0.20	3.74	0.40	0.70	0.77
7–8	Ascension	3.62	0.22	3.66	3.82	0.30	3.50	0.21	0.04	0.48
9	Atlantis	4.71	0.32	4.24	4.25	0.31	4.23	0.49	0.48	0.72
10	Atlantis II	5.32	0.76	4.14	4.17	0.65	4.12	0.46	1.18	1.32
11	Balleny	2.98	0.44	2.41	2.73	0.08	2.08	0.07	0.57	0.51
12	Birubi	4.45	0.50	3.86	3.97	0.31	3.74	0.23	0.60	0.77
13–17	Blanco	3.08	0.62	2.80	2.25	0.02	3.35	0.26	0.28	0.76
20	Boomerang	2.30	0.15	1.99	1.94	0.08	2.05	0.08	0.30	0.23
21	Bouvet	4.77	0.31	2.06	1.49	0.35	2.63	0.49	2.72	0.73
22	Bullard A	4.98	0.23	4.31	4.19	0.35	4.44	0.14	0.67	0.47
23	Bullard B	5.31	0.96	4.28	4.39	0.15	4.18	0.36	1.02	1.21

to be continued

Continued from Table A2

No.	Name	D_T/km	STD of D_T/km	D_R/km	D_{R1}/km	STD of D_{R1}/km	D_{R2}/km	STD of D_{R2}/km	D_T–D_R/km	STD of (D_T–D_R)/km
24	Chain	5.06	0.39	4.25	4.41	0.17	4.09	0.31	0.81	0.63
29	Charlie Gibbs A	3.93	0.21	3.06	2.58	0.16	3.54	0.38	0.87	0.48
30	Charlie Gibbs B	4.16	0.18	3.53	3.60	0.41	3.47	0.33	0.63	0.55
34–36	Chile	3.83	0.37	3.58	3.19	0.20	3.97	0.32	0.25	0.63
39	CIR 1 212	3.89	0.42	3.79	3.95	0.21	3.64	0.25	0.10	0.65
45	Clipperton	2.97	0.28	2.60	2.58	0.04	2.63	0.11	0.36	0.36
46	Conrad	4.70	0.37	3.89	3.64	0.32	4.14	0.28	0.81	0.67
48–49	Discovery	3.50	0.25	3.06	2.75	0.03	3.38	0.09	0.43	0.32
50	Discovery II A	4.36	0.33	3.42	2.97	0.75	3.88	0.59	0.94	1.01
51	Discovery II B	4.82	0.35	3.68	3.82	0.56	3.53	0.13	1.14	0.70
52–56	Doldrums	4.37	0.37	4.14	4.37	0.20	3.91	0.19	0.23	0.57
57	Du Toit	5.53	0.29	4.11	4.10	0.27	4.13	0.58	1.41	0.72
59	Eric Simpson	3.40	0.53	2.52	2.23	0.46	2.81	0.39	0.88	0.95
60	Euroka	4.64	0.23	4.49	4.35	0.09	4.63	0.06	0.15	0.31
61	Falkland	3.87	0.62	3.02	3.38	0.17	2.67	0.46	0.85	0.94
64–67	Garrett	3.87	0.52	2.70	2.71	0.04	2.70	0.16	1.17	0.62
70	Geelvinck	3.84	0.35	2.71	2.86	0.16	2.56	0.10	1.13	0.47
71	Gemino	2.96	0.39	3.41	3.35	0.05	3.46	0.16	0.45	0.49
72–73	GeorgeV	3.31	0.28	2.85	2.75	0.20	2.95	0.15	0.46	0.46
76–78	Gofar	3.59	0.35	2.70	2.64	0.09	2.75	0.03	0.89	0.41
82	Hayes	3.85	0.29	3.02	2.67	0.34	3.38	0.25	0.83	0.58
87	Heezen	4.51	0.94	2.46	2.63	0.11	2.30	0.05	2.04	1.02
88	Herron	2.90	0.07	2.77	2.87	0.18	2.68	0.08	0.13	0.20
89	Hillegom's Hole	2.94	0.55	2.15	2.14	0.09	2.15	0.13	0.80	0.66
90–92	Hollister	3.04	0.64	2.32	2.25	0.04	2.40	0.04	0.72	0.68
93	Indomed	3.96	0.30	3.23	3.09	0.37	3.37	0.13	0.73	0.55
94	Islas Orcadas	4.59	0.27	3.76	3.74	0.24	3.77	0.25	0.83	0.51
95–96	JanMayen	2.22	0.47	1.67	1.31	0.68	2.02	0.88	0.55	1.25
97	Kane	4.19	0.26	4.20	4.38	0.30	4.03	0.49	0.02	0.66
101	MAR 1 520	4.57	0.29	4.14	4.30	0.55	3.99	0.32	0.43	0.72
116	MAR 35S	4.02	0.23	3.66	3.90	0.20	3.43	0.37	0.35	0.52
121	Marie Celeste	4.50	0.58	3.35	3.10	0.27	3.60	0.51	1.14	0.97
122	Marion	4.96	0.35	3.15	3.00	0.58	3.31	0.90	1.81	1.09
124	Menard	3.90	0.58	2.33	2.33	0.12	2.33	0.04	1.57	0.66
127	Oceanographer	4.04	0.25	2.95	2.81	0.50	3.10	0.53	1.08	0.77
128–129	Orozco	3.47	0.37	2.63	2.35	0.06	2.92	0.08	0.83	0.45
130	Owen	4.58	0.23	4.15	4.05	0.21	4.25	0.26	0.43	0.46
135	Prince Edward	4.73	0.32	2.87	3.24	0.91	2.51	0.83	1.86	1.19
136–139	Quebrada	4.01	0.24	3.18	3.41	0.14	2.95	0.03	0.83	0.33
140–141	Raitt	3.17	0.41	2.47	2.44	0.04	2.51	0.03	0.69	0.44
143–144	Rivera	4.10	1.01	2.72	2.67	0.06	2.76	0.07	1.38	1.07
145	Romanche	5.59	0.82	3.78	3.76	0.25	3.79	0.37	1.81	1.13
147–150	Saint Paul	3.71	0.95	3.60	3.36	0.43	3.85	0.13	0.11	1.23
152	SEIR100E	3.39	0.25	2.71	2.70	0.04	2.73	0.05	0.68	0.30
153–154	SEIR107E	3.72	0.33	3.54	3.66	0.09	3.42	0.11	0.18	0.43
155	Zeehaen	4.39	0.26	3.79	3.22	0.14	4.37	0.07	0.59	0.36
156	St Vincent	2.96	0.05	2.50	2.54	0.08	2.45	0.12	0.46	0.15
158	SEIR 88E	3.59	0.43	2.58	2.56	0.08	2.61	0.03	1.00	0.48
159	SEIR 96E A	2.50	0.54	2.99	3.24	0.05	2.74	0.11	0.49	0.62
160	SEIR 96E B	3.52	0.15	2.91	2.54	0.03	3.29	0.13	0.61	0.23
162	Shaka	5.16	0.49	4.07	3.79	0.30	4.36	0.18	1.08	0.73
163–167	Siqueiros	3.30	0.42	2.67	2.58	0.04	2.76	0.02	0.64	0.45
171–175	Tasman	2.64	0.51	2.58	2.35	0.11	2.82	0.05	0.06	0.59
176	Ter Tholen	3.69	0.16	3.33	3.67	0.06	2.98	0.09	0.37	0.24
178	Tharp	4.96	0.71	2.55	2.39	0.04	2.71	0.14	2.40	0.80
180	Udintsev	4.26	0.91	3.11	2.66	0.13	3.56	0.20	1.15	1.08

to be continued

Continued from Table A2

No.	Name	D_T/km	STD of D_T/km	D_R/km	D_{R1}/km	STD of D_{R1}/km	D_{R2}/km	STD of D_{R2}/km	D_T–D_R/km	STD of (D_T–D_R)/km
181	Vacquier	3.01	0.14	2.67	2.40	0.11	2.94	0.10	0.34	0.25
182–188	Valdavia	4.45	0.49	3.55	3.75	0.27	3.35	0.40	0.90	0.82
189	Vema	5.02	0.39	4.40	4.53	0.44	4.27	0.40	0.62	0.81
190	Vema II	5.19	0.88	3.70	3.83	0.35	3.57	0.45	1.48	1.28
192	Vlamingh	3.35	0.31	2.65	2.64	0.07	2.66	0.02	0.71	0.36
195–196	Wilkes	3.11	0.35	2.85	2.76	0.10	2.94	0.04	0.26	0.42
197–198	Yaquina	3.17	0.21	2.79	2.81	0.03	2.77	0.04	0.38	0.24
200–201	Zeewolf	3.66	0.33	3.27	3.12	0.07	3.41	0.08	0.39	0.40
160	SEIR 96E B	3.52	0.15	2.91	2.54	0.03	3.29	0.13	0.61	0.23
162	Shaka	5.16	0.49	4.07	3.79	0.30	4.36	0.18	1.08	0.73
163–167	Siqueiros	3.30	0.42	2.67	2.58	0.04	2.76	0.02	0.64	0.45
171–175	Tasman	2.64	0.51	2.58	2.35	0.11	2.82	0.05	0.06	0.59
176	Ter Tholen	3.69	0.16	3.33	3.67	0.06	2.98	0.09	0.37	0.24
178	Tharp	4.96	0.71	2.55	2.39	0.04	2.71	0.14	2.40	0.80
180	Udintsev	4.26	0.91	3.11	2.66	0.13	3.56	0.20	1.15	1.08
181	Vacquier	3.01	0.14	2.67	2.40	0.11	2.94	0.10	0.34	0.25
182–188	Valdavia	4.45	0.49	3.55	3.75	0.27	3.35	0.40	0.90	0.82
189	Vema	5.02	0.39	4.40	4.53	0.44	4.27	0.40	0.62	0.81
190	Vema II	5.19	0.88	3.70	3.83	0.35	3.57	0.45	1.48	1.28
192	Vlamingh	3.35	0.31	2.65	2.64	0.07	2.66	0.02	0.71	0.36
195–196	Wilkes	3.11	0.35	2.85	2.76	0.10	2.94	0.04	0.26	0.42
197–198	Yaquina	3.17	0.21	2.79	2.81	0.03	2.77	0.04	0.38	0.24
200–201	Zeewolf	3.66	0.33	3.27	3.12	0.07	3.41	0.08	0.39	0.40

Notes: [1)] Segment No. same as in Table A1.

Table A3. Depth of ridge-transform intersections

Latitude	Longitude	Depth /km	Full rate /(mm·a^{-1})	Nodal high /nodal basin	Latitude	Longitude	Depth /km	Full rate /(mm·a^{-1})	Nodal high /nodal basin
65.269°S	175.960°W	3.11	56.70	nodal high	11.517°S	12.996°W	4.50	29.98	nodal basin
65.998°S	174.550°W	3.46	56.70	nodal high	7.077°S	12.979°W	4.89	29.51	nodal basin
64.341°S	171.130°W	2.51	56.74	nodal high	17.705°S	12.962°W	4.21	30.28	nodal basin
64.865°S	170.200°W	2.46	56.74	nodal high	22.428°S	12.890°W	3.99	30.40	nodal basin
166.100°S	62.199°W	3.25	47.58	nodal high	12.886°S	7.304 9°W	3.89	29.54	nodal basin
63.255°S	163.420°W	2.49	47.58	nodal high	22.749°S	12.806°W	3.36	30.40	nodal basin
62.440°S	161.910°W	2.49	46.71	nodal high	28.194°S	12.637°W	4.38	30.35	nodal basin
63.075°S	160.480°W	2.95	46.71	nodal high	28.823°S	12.443°W	3.70	30.19	nodal basin
62.822°S	158.360°W	3.13	45.98	nodal high	5.131 2°S	12.266°W	3.52	29.27	nodal basin
63.241°S	157.370°W	3.04	45.98	nodal high	21.352°S	11.962°W	3.74	30.34	nodal basin
62.091°S	155.760°W	2.87	64.73	nodal high	71.632°N	11.916°W	3.77	15.45	nodal basin
62.382°S	155.120°W	2.59	64.73	nodal high	22.200°S	11.801°W	4.43	30.40	nodal basin
59.460°S	151.250°W	2.34	68.94	nodal high	4.975°S	11.645°W	4.07	29.27	nodal basin
59.767°S	150.380°W	2.37	68.94	nodal high	21.217°S	11.493°W	3.47	30.34	nodal basin
57.468°S	148.020°W	2.41	71.90	nodal high	6.650 7°S	11.236°W	3.99	29.51	nodal basin
57.815°S	146.950°W	2.75	71.90	nodal high	46.977°S	10.497°W	2.70	27.44	nodal high
55.794°S	144.810°W	3.06	74.49	nodal high	49.315°S	9.842 8°W	4.22	26.90	nodal basin
57.103°S	140.270°W	4.35	74.49	nodal basin	48.940°S	8.091 2°W	3.62	26.90	nodal basin
56.108°S	139.380°W	3.31	75.45	nodal high	50.679°S	7.141 5°W	2.71	27.00	nodal high
56.339°S	138.770°W	2.59	75.45	nodal high	57.357°S	6.987 4°W	3.48	13.40	nodal high
54.119°S	136.970°W	2.25	77.89	nodal high	57.895°S	6.957°W	4.99	13.43	nodal basin
54.671°S	135.170°W	2.45	77.89	nodal high	70.982°N	6.619 1°W	3.71	15.45	nodal basin
53.755°S	134.470°W	2.64	78.82	nodal high	57.265°S	6.100 8°W	3.41	13.40	nodal high
44.444°N	130.420°W	2.38	51.06	nodal high	56.692°S	6.013 8°W	3.16	14.00	nodal high
55.410°S	127.720°W	2.69	78.82	nodal high	50.252°S	5.149 2°W	2.95	27.00	nodal high
54.821°S	127.400°W	2.63	79.02	nodal high	56.626°S	4.714 3°W	2.93	14.00	nodal high
42.992°N	126.610°W	3.54	51.06	nodal high	55.822°S	4.640 4°W	4.90	14.51	nodal basin
56.088°S	121.670°W	3.36	79.02	nodal high	54.254°S	2.418 3°W	2.77	26.90	nodal high

to be continued

Continued from Table A3

Latitude	Longitude	Depth /km	Full rate /(mm·a^{-1})	Nodal high /nodal basin	Latitude	Longitude	Depth /km	Full rate /(mm·a^{-1})	Nodal high /nodal basin
54.111°S	120.640°W	3.33	80.94	nodal basin	55.635°S	1.545 8°W	4.25	14.51	nodal basin
52.946°S	118.590°W	2.96	82.29	nodal high	55.183°S	1.541 4°W	3.39	14.50	nodal basin
54.629°S	118.430°W	2.69	80.94	nodal high	54.026°S	1.396 8°W	2.59	26.90	nodal high
53.077°S	117.690°W	2.73	82.29	nodal high	54.814°S	0.480 93°W	2.66	14.50	nodal high
49.276°S	116.630°W	3.55	85.47	nodal basin	54.981°S	0.470 24°E	1.77	12.72	nodal high
49.875°S	113.880°W	2.94	85.47	nodal high	53.632°S	3.051 5°E	4.00	12.72	nodal basin
13.312°S	112.270°W	2.85	133.99	nodal high	54.552°S	5.552 4°E	4.42	12.85	nodal basin
13.537°S	111.040°W	3.17	133.99	nodal high	53.841°S	6.644 3°E	4.33	12.85	nodal basin
8.882 3°S	109.810°W	2.87	129.79	nodal high	54.307°S	7.993 1°E	4.47	12.92	nodal basin
20.012°N	109.460°W	2.92	73.00	nodal high	52.902°S	9.928°E	4.44	12.92	nodal basin
35.098°S	109.020°W	3.97	46.42	nodal basin	53.547°S	25.206°E	4.85	13.29	nodal basin
9.180°S	108.260°W	3.20	129.79	nodal high	52.430°S	25.893°E	4.96	13.29	nodal basin
6.234 4°S	107.400°W	3.09	126.66	nodal high	52.847°S	27.818°E	5.45	13.34	nodal basin
6.296 2°S	106.900°W	2.84	126.66	nodal high	47.033°S	32.147°E	4.83	13.34	nodal basin
4.494 8°S	106.270°W	2.73	124.55	nodal high	47.340°S	33.468°E	4.88	13.22	nodal basin
18.475°N	106.220°W	2.73	73.00	nodal high	45.981°S	33.921°E	3.63	13.22	nodal basin
15.323°N	105.360°W	3.11	87.81	nodal high	46.324°S	34.905°E	3.86	13.19	nodal basin
4.726 8°S	104.650°W	3.34	124.55	nodal high	44.849°S	35.415°E	4.26	13.19	nodal basin
3.969 1°S	104.530°W	2.91	123.55	nodal high	44.143°S	39.161°E	3.69	13.03	nodal high
15.173°N	104.460°W	3.29	87.81	nodal basin	43.259°S	39.466°E	3.35	13.03	nodal high
10.101°N	104.340°W	2.57	106.28	nodal high	43.636°S	41.582°E	4.63	12.91	nodal basin
8.340 5°N	104.170°W	2.90	112.24	nodal high	42.735°S	41.805°E	4.61	12.91	nodal basin
4.042 6°S	103.790°W	3.37	123.55	nodal high	42.848°S	42.438°E	4.01	12.89	nodal basin
3.644 4°S	103.720°W	3.36	123.12	nodal high	40.877°S	42.855°E	3.97	12.89	nodal basin
10.242°N	103.570°W	3.03	106.28	nodal high	40.151°S	46.033°E	3.51	12.73	nodal high
8.500 8°N	102.880°W	3.05	112.24	nodal high	38.867°S	46.244°E	3.52	12.73	nodal high
3.806 8°S	102.610°W	3.41	123.12	nodal high	13.108°N	51.270°E	3.17	18.90	nodal basin
37.052°S	97.114°W	3.48	46.56	nodal basin	14.731°N	52.207°E	3.88	18.90	nodal basin
36.333°S	97.066°W	3.71	46.42	nodal basin	37.120°S	52.350°E	5.23	12.34	nodal basin
37.347°S	95.285°W	3.76	46.62	nodal basin	36.191°S	52.353°E	5.21	12.34	nodal basin
37.074°S	95.259°W	3.55	46.56	nodal basin	35.559°S	53.435°E	5.49	12.27	nodal basin
37.295°S	94.098°W	2.99	46.62	nodal basin	36.160°S	53.459°E	4.25	12.27	nodal basin
38.335°S	94.081°W	3.25	46.85	nodal basin	14.370°N	53.821°E	3.16	19.00	nodal basin
38.343°S	92.568°W	3.42	46.85	nodal basin	14.761°N	54.013°E	2.91	19.00	nodal basin
39.011°S	92.534°W	3.23	46.98	nodal basin	34.737°S	54.160°E	4.50	12.23	nodal basin
40.279°S	91.867°W	3.88	46.80	nodal basin	35.338°S	54.167°E	4.16	12.23	nodal basin
41.111°S	91.831°W	3.78	47.42	nodal basin	10.127°N	56.727°E	4.34	22.84	nodal basin
38.954°S	91.568°W	3.44	46.98	nodal basin	33.621°S	57.055°E	5.63	12.02	nodal basin
40.242°S	91.540°W	3.57	46.80	nodal basin	31.834°S	57.121°E	4.28	12.02	nodal high
41.259°S	91.256°W	3.65	47.45	nodal basin	12.646°N	58.351°E	4.51	22.84	nodal basin
41.111°S	91.242°W	3.96	47.42	nodal basin	31.679°S	58.437°E	4.32	11.93	nodal basin
41.188°S	90.353°W	4.38	47.45	nodal basin	31.171°S	58.448°E	4.38	11.93	nodal basin
41.335°S	90.349°W	3.99	47.47	nodal basin	29.523°S	60.700°E	5.97	11.74	nodal basin
41.244°S	89.079°W	3.57	47.47	nodal basin	30.311°S	60.804°E	5.29	11.74	nodal basin
41.419°S	89.058°W	4.05	47.48	nodal basin	17.993°S	65.073°E	3.43	35.99	nodal basin
41.311°S	87.733°W	4.20	47.48	nodal basin	12.144°S	65.699°E	3.93	31.90	nodal basin
41.515°S	87.705°W	4.64	47.51	nodal basin	13.966°S	65.875°E	3.14	33.33	nodal basin
41.303°S	85.642°W	4.32	47.51	nodal basin	11.248°S	66.171°E	3.13	31.00	nodal basin
41.541°S	85.608°W	3.95	47.54	nodal basin	10.321°S	66.300°E	4.29	30.90	nodal basin
41.438°S	84.661°W	3.92	47.54	nodal basin	20.274°S	66.347°E	3.47	38.13	nodal basin
41.601°S	84.639°W	4.41	47.56	nodal basin	11.612°S	66.437°E	4.13	31.90	nodal basin
41.531°S	83.897°W	3.97	47.56	nodal basin	16.531°S	66.626°E	3.39	35.58	nodal basin
43.084°S	83.406°W	3.78	47.82	nodal basin	9.583 9°S	66.673°E	4.69	30.95	nodal basin
43.002°S	82.685°W	3.95	47.82	nodal basin	20.047°S	66.750°E	4.23	38.13	nodal basin
45.008°S	81.923°W	3.92	48.10	nodal basin	10.819°S	66.758°E	3.10	31.00	nodal basin

to be continued

Continued from Table A3

Latitude	Longitude	Depth /km	Full rate /(mm·a^{-1})	Nodal high /nodal basin	Latitude	Longitude	Depth /km	Full rate /(mm·a^{-1})	Nodal high /nodal basin
44.478°S	78.347°W	3.57	48.10	nodal basin	13.353°S	66.814°E	3.83	33.33	nodal basin
45.867°S	77.905°W	2.93	48.27	nodal basin	9.879 8°S	66.883°E	3.94	30.90	nodal high
45.646°S	76.864°W	3.96	48.27	nodal basin	17.011°S	66.951°E	3.80	35.99	nodal basin
46.006°S	76.715°W	3.25	48.30	nodal basin	20.416°S	66.964°E	3.79	38.48	nodal basin
45.819°S	76.008°W	3.28	48.30	nodal basin	0.433 37°S	67.011°E	3.43	29.80	nodal basin
15.382°N	46.632°W	5.00	23.57	nodal basin	0.112 8°S	67.255°E	3.61	29.80	nodal basin
23.833°N	46.303°W	5.05	23.43	nodal basin	1.415 1°S	67.395°E	3.52	29.87	nodal basin
23.617°N	44.923°W	5.63	23.43	nodal basin	16.050°S	67.427°E	3.88	35.58	nodal basin
12.626°N	44.876°W	4.27	24.41	nodal basin	20.107°S	67.539°E	3.65	38.48	nodal basin
15.192°N	44.855°W	4.98	23.57	nodal basin	1.070 5°S	67.676°E	3.24	29.87	nodal basin
12.542°N	44.100°W	4.55	24.41	nodal basin	20.450°S	67.753°E	3.08	38.40	nodal basin
10.845°N	43.715°W	5.18	24.98	nodal basin	7.864 4°S	67.848°E	3.57	30.63	nodal high
30.101°N	42.686°W	4.65	22.40	nodal basin	7.121 2°S	67.940°E	3.86	30.17	nodal high
30.025°N	41.989°W	4.82	22.40	nodal basin	2.665 3°S	67.960°E	3.71	30.40	nodal basin
10.731°N	40.883°W	5.04	24.98	nodal basin	3.234 3°S	68.000°E	3.33	30.48	nodal basin
8.844 2°N	40.491°W	5.00	25.56	nodal basin	6.091 4°S	68.004°E	3.46	31.14	nodal basin
8.810 4°N	39.461°W	4.18	25.56	nodal basin	2.885 7°S	68.237°E	3.41	30.48	nodal basin
8.185 7°N	39.461°W	5.06	25.74	nodal basin	20.201°S	68.238°E	2.98	38.40	nodal basin
33.773°N	39.106°W	3.59	21.65	nodal basin	2.188 5°S	68.273°E	3.51	30.40	nodal basin
7.700 3°N	38.026°W	5.09	25.89	nodal basin	4.135 9°S	68.273°E	3.82	30.78	nodal basin
8.168 8°N	38.013°W	4.62	25.74	nodal basin	8.224 6°S	68.281°E	4.36	30.95	nodal high
33.515°N	37.861°W	3.73	21.65	nodal basin	7.435 6°S	68.302°E	3.44	30.63	nodal high
35.237°N	36.215°W	4.01	21.27	nodal basin	5.009 5°S	68.393°E	3.66	31.00	nodal basin
7.362 7°N	36.050°W	4.80	26.00	nodal basin	6.552 2°S	68.529°E	4.00	30.17	nodal high
7.725 7°N	36.025°W	4.28	25.89	nodal basin	3.655 1°S	68.690°E	3.35	30.78	nodal basin
52.707°N	35.105°W	3.63	21.73	nodal basin	5.346 1°S	68.714°E	4.09	31.14	nodal basin
35.069°N	35.020°W	4.46	21.27	nodal basin	4.560 7°S	68.822°E	3.33	31.00	nodal basin
7.185 4°N	34.674°W	4.58	26.08	nodal basin	22.877°S	69.138°E	3.18	40.99	nodal basin
7.438 6°N	34.657°W	4.39	26.00	nodal basin	22.680°S	69.499°E	3.22	40.99	nodal basin
7.168 5°N	33.910°W	4.07	26.08	nodal basin	33.755°S	77.343°E	3.72	60.26	nodal basin
3.872°N	32.547°W	4.47	26.96	nodal basin	37.896°S	77.957°E	1.76	62.10	nodal high
52.540°N	31.765°W	4.09	21.73	nodal basin	38.870°S	78.082°E	2.09	62.70	nodal high
52.158°N	31.734°W	3.47	21.83	nodal basin	33.175°S	78.128°E	3.01	60.26	nodal high
3.905 8°N	31.572°W	4.69	26.96	nodal basin	35.659°S	78.203°E	3.10	61.41	nodal basin
52.044°N	30.034°W	3.96	21.83	nodal basin	37.012°S	78.217°E	2.02	62.02	nodal high
0.786 52°N	29.892°W	3.16	27.71	nodal basin	37.664°S	78.267°E	1.77	62.10	nodal high
1.027 1°N	27.714°W	4.56	27.71	nodal basin	38.489°S	78.531°E	2.90	62.70	nodal high
0.811 85°N	27.663°W	4.73	27.77	nodal basin	35.121°S	78.824°E	2.74	61.41	nodal high
0.921 59°N	26.410°W	4.92	27.77	nodal basin	36.391°S	79.148°E	2.90	62.02	nodal basin
0.664 11°N	26.313°W	4.54	27.83	nodal basin	41.889°S	79.944°E	3.20	64.35	nodal basin
60.912°S	25.490°W	5.70	12.26	nodal basin	41.129°S	80.85°E	3.43	64.35	nodal basin
0.756 97°N	25.481°W	5.02	27.83	nodal basin	43.034°S	83.547°E	3.76	65.60	nodal basin
0.545 93°N	25.456°W	4.42	27.88	nodal basin	40.918°S	85.941°E	3.61	65.60	nodal basin
0.617 68°N	25.004°W	4.12	27.88	nodal basin	42.142°S	88.110°E	2.39	66.47	nodal high
1.235 3°S	24.582°W	4.58	28.27	nodal basin	41.696°S	88.706°E	2.59	66.47	nodal high
60.798°S	19.601°W	4.94	12.26	nodal basin	46.012°S	95.710°E	3.45	68.69	nodal basin
60.303°S	19.379°W	4.19	12.80	nodal basin	46.599°S	96.024°E	2.61	68.82	nodal basin
60.299°S	18.757°W	4.08	12.80	nodal basin	46.278°S	96.271°E	3.23	68.82	nodal basin
59.186°S	17.984°W	5.33	12.99	nodal basin	45.370°S	96.500°E	3.40	68.69	nodal basin
35.576°S	17.689°W	3.74	29.60	nodal basin	48.265°S	99.375°E	3.03	69.46	nodal high
38.430°S	17.069°W	3.12	29.00	nodal high	47.197°S	110.320°E	2.82	69.46	nodal high
40.380°S	16.875°W	3.12	28.90	nodal basin	49.345°S	116.110°E	3.72	70.11	nodal high
0.182 93°N	16.689°W	3.99	28.27	nodal basin	48.839°S	116.520°E	4.36	70.11	nodal basin
39.873°S	16.554°W	3.77	28.98	nodal basin	48.876°S	116.660°E	3.42	70.12	nodal basin
40.291°S	16.449°W	3.54	28.90	nodal basin	48.302°S	117.060°E	2.98	70.12	nodal high

to be continued

Continued from Table A3

Latitude	Longitude	Depth /km	Full rate /(mm·a^{-1})	Nodal high /nodal basin	Latitude	Longitude	Depth /km	Full rate /(mm·a^{-1})	Nodal high /nodal basin
38.341°S	16.377°W	4.67	29.00	nodal high	50.425°S	114.010°E	3.42	70.35	nodal high
59.143°S	16.332°W	4.30	12.99	nodal basin	49.832°S	114.400°E	4.43	70.35	nodal basin
58.452°S	15.950°W	5.82	13.43	nodal basin	50.159°S	120.090°E	4.33	70.19	nodal basin
39.747°S	15.912°W	3.23	28.98	nodal high	49.289°S	120.490°E	4.10	70.19	nodal basin
1.577 2°S	15.862°W	4.50	28.58	nodal basin	49.363°S	120.780°E	3.94	70.20	nodal basin
34.247°S	15.229°W	3.94	29.71	nodal basin	48.869°S	121.060°E	4.55	70.20	nodal basin
35.192°S	15.136°W	3.23	29.60	nodal high	49.715°S	121.440°E	4.74	70.13	nodal basin
11.906°S	14.988°W	3.65	29.98	nodal basin	49.005°S	121.670°E	4.04	70.13	nodal basin
33.546°S	14.629°W	3.34	29.70	nodal basin	49.696°S	123.600°E	4.24	69.97	nodal basin
32.356°S	14.515°W	3.23	29.89	nodal basin	48.808°S	123.990°E	4.36	69.97	nodal basin
34.124°S	14.503°W	3.73	29.71	nodal basin	49.869°S	125.980°E	4.21	69.76	nodal basin
14.215°S	14.465°W	3.06	30.02	nodal basin	48.690°S	126.340°E	4.59	69.76	nodal basin
16.418°S	14.334°W	4.02	30.00	nodal basin	49.949°S	127.150°E	4.18	69.62	nodal basin
33.491°S	14.321°W	4.00	29.70	nodal basin	48.814°S	127.530°E	4.28	69.62	nodal basin
17.908°S	14.064°W	3.20	30.28	nodal basin	50.332°S	139.690°E	3.35	67.49	nodal basin
25.733°S	14.000°W	3.88	30.32	nodal basin	51.899°S	139.750°E	3.25	67.49	nodal high
26.628°S	13.815°W	3.14	30.15	nodal basin	51.875°S	140.830°E	3.79	67.30	nodal basin
24.957°S	13.794°W	4.36	30.35	nodal basin	53.985°S	140.980°E	2.96	67.30	nodal high
29.27°S	13.713°W	3.83	30.13	nodal basin	54.794°S	143.970°E	2.97	66.50	nodal basin
22.973°S	13.659°W	4.14	30.40	nodal basin	54.263°S	144.220°E	2.87	66.50	nodal basin
25.666°S	13.616°W	3.98	30.32	nodal basin	54.763°S	146.380°E	2.51	66.05	nodal high
14.079°S	13.612°W	3.42	30.02	nodal basin	55.719°S	146.630°E	2.23	66.05	nodal basin
26.561°S	13.587°W	3.51	30.15	nodal basin	55.651°S	147.220°E	2.99	65.82	nodal high
7.44°S	13.477°W	4.97	29.54	nodal basin	57.527°S	147.710°E	3.11	65.82	nodal basin
24.822°S	13.333°W	4.09	30.35	nodal basin	57.478°S	148.370°E	2.87	65.51	nodal high
47.619°S	13.321°W	3.43	27.44	nodal high	58.145°S	148.580°E	2.88	65.51	nodal high
32.094°S	13.249°W	3.70	29.89	nodal basin	58.033°S	148.950°E	2.67	65.29	nodal high
16.186°S	13.207°W	3.60	30.00	nodal basin	59.669°S	149.810°E	3.23	65.29	nodal high
28.304°S	13.203°W	3.97	30.35	nodal basin	59.484°S	150.330°E	3.01	65.29	nodal basin
0.914 5°S	13.160°W	4.94	28.58	nodal basin	60.520°S	150.850°E	3.18	65.29	nodal basin
28.945°S	13.059°W	3.91	30.19	nodal basin	59.940°S	153.630°E	3.54	64.50	nodal basin
29.123°S	13.038°W	4.89	30.13	nodal basin	62.939°S	156.270°E	2.26	64.50	nodal high